Probing the band structure of the strongly correlated antiferromagnet $NiPS_3$ across its phase transition

Benjamin Pestka[†],[1] Biplab Bhattacharyya[†],[1] Miłosz Rybak[†],[2] Jeff Strasdas,[1] Adam K. Budniak,[3] Adi Harchol,[3] Marcus Liebmann,[1] Niklas Leuth,[1] Honey Boban,[4] Vitaliy Feyer,[4] Iulia Cojocariu,[4,5,6] Daniel Baranowski,[4,7] Simone Mearini,[4] Lutz Waldecker,[8] Bernd Beschoten,[8] Christoph Stampfer,[8] Yaron Amouyal,[9] Lukasz Plucinski,[4] Efrat Lifshitz,[3] Krzysztof Wohlfeld,[10] Magdalena Birowska,[10] and Markus Morgenstern[*1]

[1] *II. Institute of Physics B and JARA-FIT, RWTH-Aachen University, 52074 Aachen, Germany*
[2] *Department of Semiconductor Materials Engineering Faculty of Fundamental Problems of Technology Wrocław University of Science and Technology Wybrzeże Wyspiańskiego 27, 50-370 Wrocław, Poland*
[3] *Schulich Faculty of Chemistry, Solid State Institute, Russell Berrie Nanotechnology Institute, Technion, Haifa 3200003, Israel*
[4] *Forschungszentrum Jülich, Peter Grünberg Institute (PGI-6), 52425 Jülich, Germany*
[5] *Physics Department, University of Trieste, Trieste, 34127 Italy*
[6] *Elettra – Sincrotrone Trieste S.C.p.A., S.S. 14 km 163.5, Trieste, 34149 Italy*
[7] *Physical and Computational Sciences, Directorate and Institute for Integrated Catalysis, Pacific Northwest National Laboratory, Richland, WA 99354, USA*
[8] *2nd Institute of Physics and JARA-FIT, RWTH-Aachen University, Aachen 52074, Germany*
[9] *Department of Materials Science and Engineering, Technion – Israel Institute of Technology, Haifa 3200003, Israel*
[10] *Institute of Theoretical Physics, Faculty of Physics, University of Warsaw, Pasteura St. 5, 02-093 Warsaw, Poland*

(Dated: January 6, 2026)

Abstract

$NiPS_3$ is an exfoliable van-der-Waals intralayer antiferromagnet with zigzag-type spin arrangement. It is distinct from other $TMPS_3$ (TM: transition metal) materials by optical excitations into a strongly correlated state that is tied to the magnetic properties. However, the related, fundamental band structure across the antiferromagnetic phase transition has not been probed yet. Here, we use angular-resolved photoelectron spectroscopy with μm resolution in combination with DFT+U calculations for that purpose. We identify a characteristic band shift across T_N. It is attributed to bands of mixed Ni and S character related to the superexchange interaction of Ni $3t_{2g}$ orbitals. Moreover, we find a structure above the valence band maximum with little angular dispersion that could not be reproduced by the calculations. The discrepancy suggests the influence of many-body interactions beyond the DFT+U approximations in striking contrast to the results on $MnPS_3$ and $FePS_3$, where these calculations were sufficient for an adequate description.

[†]These authors contributed equally to this work.
[*]Corresponding author: M. Morgenstern, Email: mmorgens@physik.rwth-aachen.de

I. INTRODUCTION

Van der Waals (vdW)-type two-dimensional (2D) ferromagnets (FMs) and antiferromagnets (AFMs) [5–10] enrich the possibilities for spintronics, magneto-optical devices and magnetic sensors [11–15]. This is related to the fact that the 2D magnetism can be tuned via magnetic fields, electrostatic gating, current pulses, strain, light, ion intercalation, proximity and moiré lattices [11, 13, 16–20] as well as due to the relatively strong magneto-electric, magneto-elastic and magneto-optic couplings [21–26]. Moreover, these materials enable a novel access to fundamental questions in 2D magnetism such as the Berezinskii–Kosterlitz–Thouless (BKT) transition or proximity-induced modifications of the magnetization [7, 13–15, 19, 27–30].

A unique type are transition metal (TM) phosphorus trisulfides $TMPS_3$ [31, 32]. In contrast to other vdW magnets, they are intralayer AFMs and, moreover, rather directly realize the three most prominent classes of 2D magnetism (Ising, XY, Heisenberg) [4, 33, 34]. Hence, the materials provide a versatile platform to study 2D AFM properties. The $TMPS_3$ materials are semiconductors with a layered honeycomb structure of the TM^{2+} atoms, each surrounded by covalently bonded $(P_2S_6)^{4-}$ bipyramids (Fig. 1a). The magnetism arises from the competition between direct exchange interactions between neighboring TM atoms and indirect superexchange mediated by S and P atoms [34–36]. Depending on the relative strength of the competitive interactions, various long-range AFM orders have been found, dubbed zigzag, Néel, and stripy AFM order [31, 37].

$NiPS_3$ stands out since it exhibits significant spin-

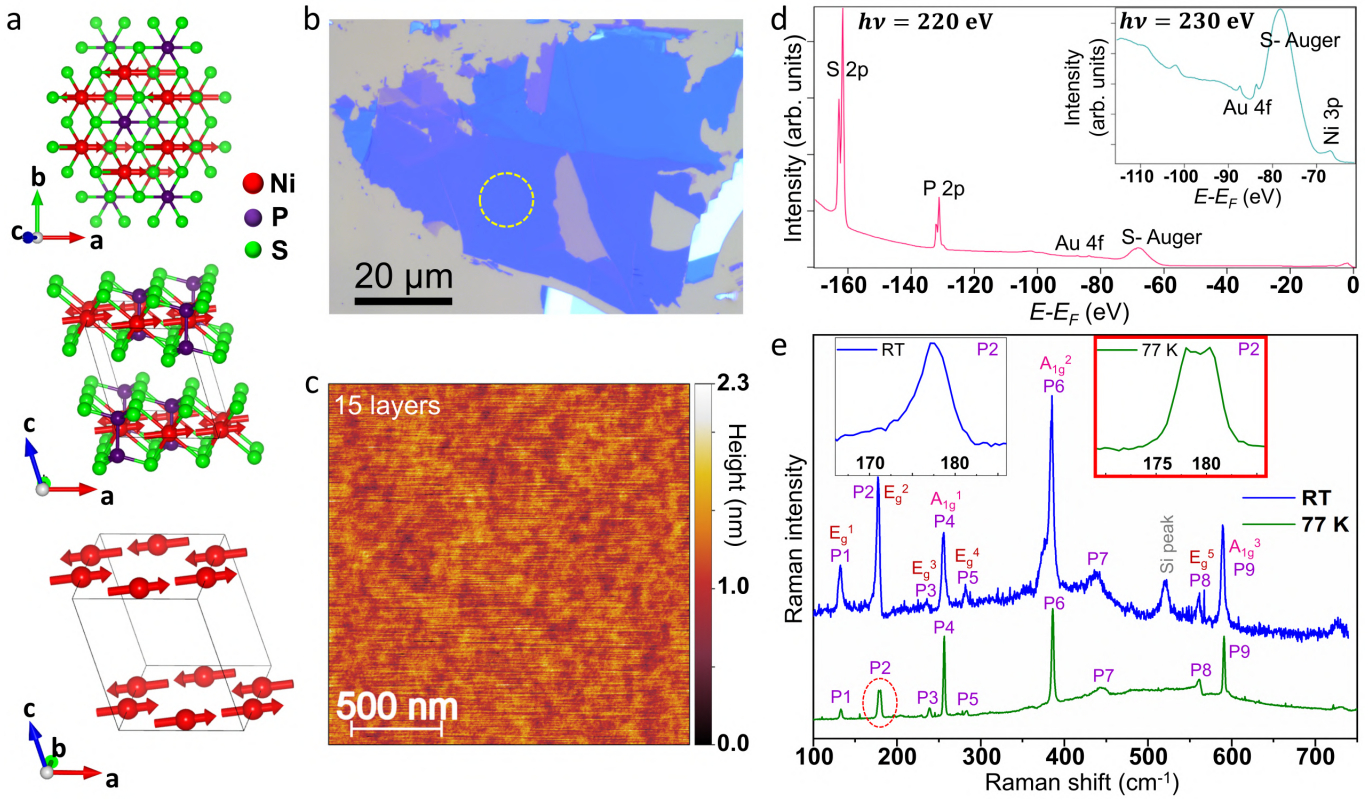

Figure 1. **Characterization of exfoliated $NiPS_3$ flakes.** (a) Atomic top view (top image) and side view (middle image) of two layers of $NiPS_3$, red arrows: spins of the Ni atoms, bottom image: only the Ni atoms highlighting their honeycomb atomic and zigzag-type AFM magnetic arrangement. (graphics made by VESTA [1]). (b) Optical microscope image of an exfoliated $NiPS_3$ on a Au/Ti/SiO_2/Si substrate. The yellow dashed circle marks the 15 layer thick area used for ARPES. (c) Atomic force microscopy image of the flake area probed by ARPES (rms roughness: 0.14 nm). (d) XPS of the same 15 layer area after the ARPES measurements, $h\nu = 220$ eV, peaks are labeled by element and atomic core level orbital. Inset: XPS at $h\nu = 230$ eV exposing the Ni 3p peak by shifting the otherwise overlapping S-Auger peak to lower $E - E_F$. (e) Raman spectra at room temperature (RT) and 77 K ($T_N = 155$ K) labeled according to their symmetries and as P1 to P9 for easier description. A Si peak originating from the substrate is also labeled [2]. The peak around 730 cm^{-1} is due to a second-order Raman mode [2]. Insets: Zoom into the area of P2 with apparent peak splitting at 77 K caused by magnon-phonon interaction [3, 4].

charge coupling, leading to spin-correlated excitons whose origin is actively debated. The excitons display layer-dependent characteristics and polarization properties correlated with the material's magnetism [21, 24, 25, 38–45]. This might enable novel optomagnonic interconnects (Supplementary section S1), e. g. via the ultra-sharp exciton peak observed at approximately 1.47 eV [3, 33, 38, 46]. It has also been shown that the properties of this exciton peak can only be described correctly by calculations employing muliplet-type exact diagonalization [42]. Moreover, the magnetic interactions are surprisingly dominated by a third nearest neighbor AFM exchange coupling due to a substantial overlap of p- and d-orbitals along the corresponding Ni-S-P-S-Ni interaction path [33–35, 47]. This leads to an intralayer AFM zigzag order as the ground state below the bulk Néel temperature $T_N \approx 155$ K, where the spins are oriented mostly in-plane along the zigzag direction (Fig. 1a) with a slight canting out-of-plane by ∼8° [21]. In monolayer form, the long-range magnetic order is most likely suppressed potentially leading to a BKT transition [4, 30]. This behavior aligns with descriptions based on a highly anisotropic XXZ model [31, 48].

The magnetic ordering of $NiPS_3$ has already been probed by multiple methods [3, 4, 24, 25, 38, 47, 51–53], but none of them is sensitive to details of the band structure, which has only been probed at room temperature so far, i. e. above T_N, using angular resolved photoelec-

Material	AFM order	Bandgap (eV)	T_N (K)	U_{eff} (eV)	Band shift across T_N
$NiPS_3$(this work)	zigzag (XY-like)	1.8	155	1.6	mixed Ni 3d/S 3p band, extra band at valence band maximum
$FePS_3$ [49]	zigzag(Ising-like)	1.5	117	1.2	S 3p-, Fe 3d- and P 3p-type bands
$MnPS_3$ [50]	Néel	2.94	78	1.8	Mn 3d dominated band

Table I. $TMPS_3$ properties, T_N: Néel temperature, U_{eff}: selected effective Hubbard parameter of the transition metal d levels for the DFT+U calculations that reproduces the experimental μ-ARPES data most favorably, band shifts across T_N are determined by μ-ARPES and assigned to elements and orbitals by comparison with the band structures from DFT+U calculations.

tron spectroscopy (ARPES) [42, 54, 55]. Here, we provide band structure mapping by ARPES at variable temperature T above and below T_N leveraging the approach that we recently developed for the isostructural $MnPS_3$ and $FePS_3$ [49, 50]. We prevent sample charging due to photoelectrons, that often appears for semiconductors at low T [56–60], by exfoliating thin films of $NiPS_3$ onto a conductive Au film deposited on Si/SiO_2, itself necessary for identifying the flakes optically. The resulting band structure is compared with density functional theory calculations (DFT+U) enabling the identification of the elemental and orbital character of the different bands and revealing an optimal Hubbard parameter $U_{eff} = 1.6\,eV$. Most importantly, we observe a pronounced band shift across T_N for a valence band identified as a mixed Ni 3d/S 3p band that could be attributed to a next nearest neighbor superexchange path. Moreover, we reveal an additional band feature in ARPES that appears above the valence band maximum, but could not be reproduced by the DFT+U calculations. We believe that it testifies the strong correlations in $NiPS_3$ compared to $MnPS_3$ and $FePS_3$ in line with the optical results [21, 24, 25, 38, 39].

Since the comparison between these three materials is crucial for the missing assignment of this band, we provide such a comparison in table I. In particular, the selected U_{eff} values are rather similar for all three materials as expected by the identical chemical environment of the transition metal 3d levels.

II. RESULTS AND DISCUSSION

$NiPS_3$ single crystals are synthesized by the vapor transport method. Flakes are subsequently exfoliated by the scotch tape method onto Au/Ti covered Si/SiO_2 at 60° C, shortly after the substrate was cleaned by plasma ashing [50] (Materials and Methods). Flakes with appropriate thickness and lateral size are identified using optical and atomic force microscopy (Fig. 1b-c). Typically, these flakes exhibit various thicknesses being most thin at the rim. In this paper, we studied a 15 layer thick area with a lateral size of $17 \times 21\,\mu m^2$ as marked in Fig. 1b. Atomic force microscopy reveals a rms roughness of 0.14 nm and no obvious contaminations in that area (Fig. 1c). The relatively small thickness is crucial to avoid charging during μ-ARPES at low temperature as detected, e. g. for 45 layers at 90 K, where all bands are shifted downwards by 0.3 eV.

Figure 1d displays X-ray photoelectron spectroscopy (XPS) data of the 15 layer area. All components of $NiPS_3$ appear as core level peaks [61–63] as well as a S Auger peak [64]. The latter shifts with respect to the other peaks by changing the photon energy $h\nu$ exposing the Ni 3p peak [65]. A small contribution from the spin-split Au 4f peaks [65] is also visible likely originating from the substrate due to the relatively large spot of the photon beam on the sample (diameter: 15 μm) at the large $h\nu$ for XPS.

The antiferromagnetic phase transition of the exfoliated $NiPS_3$ flakes is verified by Raman spectroscopy (Fig. 1e). Due to the nearly realized D_{3d} intralayer point group symmetry [2], $NiPS_3$ has eight major Raman-active phonon modes, all visible in our Raman spectra with frequencies in good agreement with the literature [2–4, 68]. We reproduce three signatures that have previously been assigned to the AFM phase transition [3, 4]. Firstly, a broad 2-magnon scattering peak, centered at $\sim$530 cm^{-1}, appears below T_N at 77 K and is absent at room temperature (RT) [4]. Secondly, the peak P2 caused by in-plane vibrations of the Ni atoms splits into a double peak (insets, Fig. 1e) as attributed to a pronounced magnon-phonon coupling [3, 4]. Thirdly, the peak P8, caused by an in-plane E_g-type vibration of the $(P_2S_6)^{4-}$ bipyramids, develops a Fano-resonance line shape below T_N due to an interference between the phonon excitation and the continuum of 2-magnon excitations [69]. These three fingerprints confirm the AFM phase transition in our $NiPS_3$ flakes.

Figure 2 shows the main result of this work, namely a band shift across T_N near the $\overline{\Gamma}$ point. We present the raw ARPES data (a–b), the data after box-type smoothing (c, only the energy distribution curve (EDC) is shown), after additional background subtraction (d–f) and angularly averaged in $\boldsymbol{k}$-space around the $\overline{\Gamma}$ point (g–h). Al-

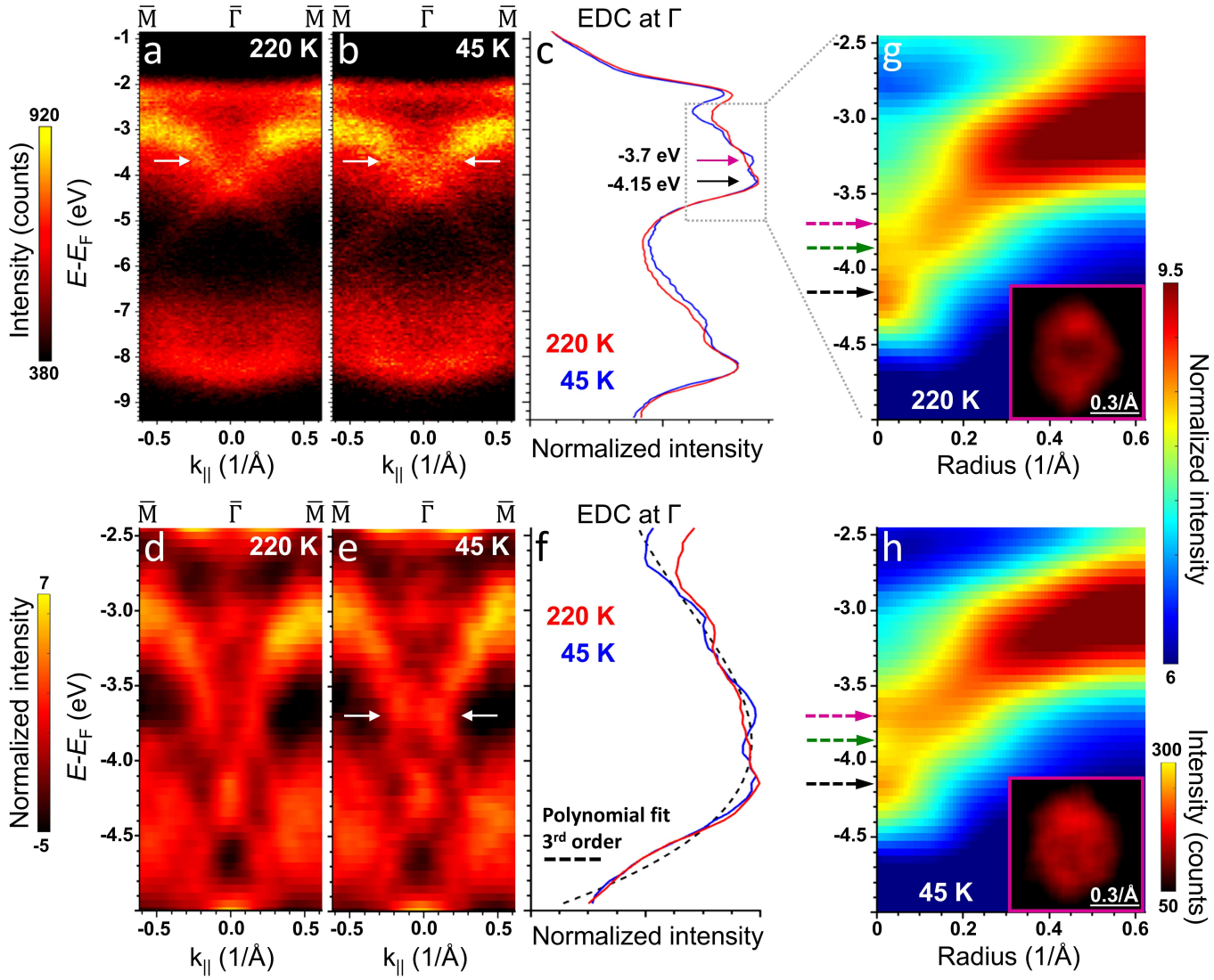

Figure 2. **Electronic band structure change of $NiPS_3$ across T_N.** (a), (b) Raw ARPES data above (220 K) and below (45 K) $T_N = 155$ K, white arrows point to the changes highlighted in c–h, $h\nu = 60$ eV, $\overline{M\Gamma M}$ direction. (c) Intensity plots from a–b at $k_{||} = 0$/Å after smoothing by box filters (100 meV/two pixels in E, 0.041/Å/5 pixels in $k_{||}$). An additional peak appears at $E - E_F = -3.7$ eV close to the peak at -4.15 eV, which is present at both T (arrows). (d), (e) Smoothed ARPES data from a–b after subtracting a 3rd-order polynomial background, adapted for each $k_{||}$ to the whole displayed $E - E_F$ range as shown exemplarily in f. White arrows (same energy as in a–b) mark the most prominent change. (f) Zoom into c (blue and red curve) with a 3^{rd} order polynomial fit to the blue curve (dashed line). (g), (h) Angular averaged intensity of the smoothed data in the energy range marked by a box in c, (g) above T_N, (h) below T_N, black, pink arrows: same energies as in c, green arrow: energy of intensity at 220 K that likely shifts upwards at 45 K. Insets: (k_x, k_y) plots of the smoothed photoelectron intensity at $E - E_F = -3.7$ eV (green, pink arrows in main image) after background subtraction. The center is Γ. (a)-(c), respectively (d)-(f), share the same energy axis.

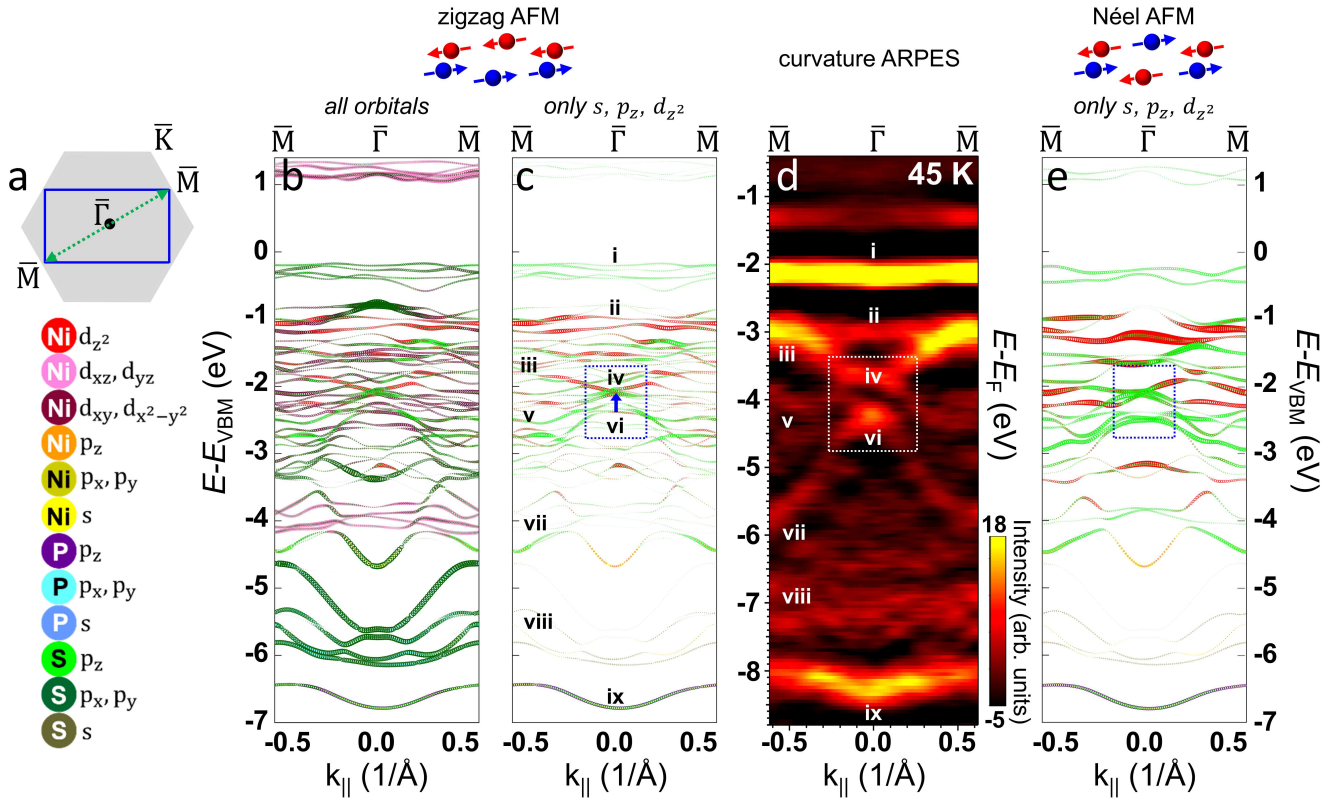

Figure 3. **Identifying the orbital character of the bands.** (a) Surface projected Brillouin zone of the atomic geometry (grey hexagon) with high symmetry points marked and the magnetic zigzag structure (blue rectangle). (b) Band structure of $NiPS_3$ in the AFM zigzag configuration as sketched on top, DFT+U calculations unfolded to the hexagonal, atomic Brillouin zone sketched in a [66], $U_{\text{eff}} = 1.6\,\text{eV}$, $k_z = 0.1/\text{Å}$, $\overline{\text{M}\Gamma\text{M}}$ direction as marked in a. The energy is related to the valence band maximum E_{VBM}. The atomic orbital contributions of each state are depicted by overlapping, colored circles with diameter proportional to the contribution (color code on the left, diameter of dark green circles at $E - E_{\text{VBM}} \approx -5\,\text{eV}$ are $\sim 100\,\%$. (c) Same as (b) but only showing the s, p_z and d_{z^2} orbital contributions in accordance with simplified ARPES selection rules [67]. Blue arrow marks the position of band change observed in Fig. 2 (d) ARPES curvature plot, $h\nu = 60$ eV, $T = 45\,\text{K}$, $\overline{\text{M}\Gamma\text{M}}$ direction. Labels i-ix: similar band features in c (DFT+U) and d (ARPES) (see text). Dashed rectangles: area of the magnetically induced band shift (Fig. 2). (e) Same as c for the Néel configuration as sketched on top. Figures b–e share the same scaling of the energy. The DFT + U data are adapted to the ARPES data by a rigid shift optimizing the overlap of structures i-ix.

ready the raw data (Fig. 2a–b) exhibit a slightly enhanced intensity below T_{N} in between the white arrows. This change can be identified as an additional peak in the EDC at $\bar{\Gamma}$ after mild smoothing (upper arrow, Fig. 2c) implying a state at $E - E_{\text{F}} = -3.7\,\text{eV}$ below T_{N} (E: energy, E_{F}: Fermi energy as probed on Au). A polynomial background subtraction (Fig. 2f) increases the visibility of that peak. The resulting energy vs. wave vector display of the photoelectron intensity (Fig. 2d–e) reveals that the peak belongs to a rather flat band extending up to an in-plane wave vector $|\boldsymbol{k}_{\parallel}| \approx 0.15/\text{Å}$, where it merges with upwards dispersing bands. These features are corroborated by the angulary averaged data in $\boldsymbol{k}_{\parallel}$ space (Fig. 2g–h). The band at $E - E_{\text{F}} = -3.7\,\text{eV}$ is again visible below T_{N} (Fig. 2h, pink arrow). It shifts downwards by roughly 150 meV above T_{N} (Fig. 2g, green arrow), nearly merging with the band at $E - E_{\text{F}} = -4.15\,\text{eV}$ (Fig. 2g-h, black arrows). The insets finally show the two-dimensional $\boldsymbol{k}_{\parallel}$ plots at that energy exhibiting a ring above T_{N} due to the upwards dispersing bands and a full circle below T_{N} due to the additional flat band. The upwards dispersing bands visible in the main image are also slightly less steep below T_{N}.

One might suspect that the downwards shift is related to a distinct structural phase transition or to a continuous thermal contraction of the $NiPS_3$ crystal. However,

there is no structural phase transition in that temperature range as known from neutron diffraction [48], while shifts of electronic states by thermal contraction are less than 50 meV between 220 K and 45 K as deduced from electronic Raman spectroscopy [21]. We confirmed this by DFT+U calculations using the lattice parameters deduced from neutron diffraction at 295 K and 2 K to scale the lattice parameters in DFT+U. These calculations did not reveal any band shifts larger than 50 meV as well (not shown), in particular in the energy range where the band structure change was observed in Fig. 2.

Next, we compare the ARPES data with DFT+U calculations of the magnetic ground state (AFM zigzag type) and other magnetic configurations (AFM Néel and disordered). This aims to identify the elemental and orbital character of the different bands, in particular the ones that are changing across T_{N}. We started by selecting the proper Hubbard U_{eff} parameter (DFT+U) by detailed comparison with the experimental data. The best match for the ARPES data at $h\nu = 60\,\mathrm{eV}$ and $T = 45\,\mathrm{K}$ is found for $U_{\mathrm{eff}} = 1.6\,\mathrm{eV}$ (Suppl. section S3) and $k_z = 0.1/\mathrm{\AA}$ (Suppl. section S4). The k_z selection is corroborated by photon energy dependent ARPES data that are successfully compared with the k_z dependent DFT+U data employing an inner potential of 12.1 eV (Suppl. Fig. S5).

The band structure is additionally unfolded to the atomic Brillouin zone (grey hexagon in Fig. 3a) [66] (Suppl. Fig. S2). This reflects the fact that the enlarged periodicity by AFM order is barely imprinted in the wave functions [70]. Indeed, (k_x, k_y) maps of the ARPES data did not show any patterns reminiscent of the magnetic Brillouin zone, but only of the hexagonal, geometric one (Suppl. section S2). Figure 3c shows the same DFT+U data as in b, but after selecting only the orbital contributions s, p_z, and d_{z^2} within a frame where the z-direction is pointing perpendicular to the layers. According to simplified selection rules assuming plane waves as final states [67], these orbital contributions are excited preferably for our light polarization geometry [50]. Orbital contributions to the different bands beyond the simplified selection rules are analyzed in Suppl. section S5 with the results partially included in the following discussion. Figure 3e shows the same selection of bands for the Nèel configuration which is not realized in $NiPS_3$. This additional band structure serves to identify bands that are changing with the magnetic arrangement of the atoms. For the same purpose, we also provide the calculated band structure of a disordered magnetic configuration in Suppl. Fig. S11. Finally, Fig. 3d shows the ARPES curvature data below T_{N}. The curvature is used for better visibility of the various features (Suppl. section S12). We always cross-check with the raw data as in Fig. 2 to corroborate that a feature is not an artifact of the curvature derivation.

Multiple features are similar between the ARPES results (Fig. 3d) and the DFT+U data of the zigzag configuration (Fig. 3c) as labeled by i-ix. The bright feature (i) and the nearly parabolic feature (ix) are used to align the Fermi level of the ARPES data to the DFT+U band structure. The additional structure in ARPES at $E - E_{\mathrm{F}} \approx -1.3\,\mathrm{eV}$ is discussed below. The band (i) has a dominating S 3p character with contributions from Ni $3\mathrm{d}_{xz,\,yz,\,xy,\,x^2-y^2}$ (Suppl. Fig. S6). It is rather flat in calculation and experiment. The lowest energy band (ix) has a parabolic dispersion close to $\overline{\Gamma}$ in both cases and a mixed P $3\mathrm{p}_z$ and S 3p character. This band appears quite similarly for $MnPS_3$ and $FePS_3$ [49, 50]. It is slightly lower in the DFT+U data than in the ARPES data. This is probably due to the facts that firstly k_z moves upwards with decreasing $E - E_{\mathrm{F}}$ in ARPES at constant $h\nu$ and secondly this band moves upwards with increasing k_z in the DFT+U data (Suppl. Figs. S4/S5). At slightly larger $E - E_{\mathrm{F}}$ are bands with nearly exclusive S $3\mathrm{p}_{x,y}$ character (viii) that are barely visible in ARPES in accordance with the simplified selection rules [67]. The remaining features ii-vii exhibit a mixed Ni 3d/S 3p character. In ARPES, they are dominated by a large cross-type structure gapped at $\overline{\Gamma}$ (iv,vi) with a rather flat band on top (ii). A flat band of strong Ni $3\mathrm{d}_{z^2}$ character (ii) and a gapped crossing of mixed character (iv,vi) are also visible in DFT+U. Other features are more subtle and partially distinct such as the relatively steep lower part of the cross from vi to vii in ARPES which is not continuous across the whole energy range in DFT+U. Nevertheless, the agreement in the whole energy range below $E - E_{\mathrm{F}} = -1.5\,\mathrm{eV}$ is rather satisfactory regarding the fact that the band structure of the calculation was only rigidly shifted for adaption.

This importantly implies that the magnetically induced band shift identified in Fig. 2 is at the gapped crossing of feature (iv) and (vi), more precisely it is the upper part (iv) at $E - E_{\mathrm{F}} = -3.7\,\mathrm{eV}$ around $\overline{\Gamma}$ in the ARPES data (Fig. 3d). Accordingly, it is at $E - E_{\mathrm{VBM}} = -2.2\,\mathrm{eV}$ in the DFT+U data (arrow in Fig. 3c). Consistently, these band structure features exhibit a relatively strong change in DFT+U data, if the magnetic structure is changed. For the zigzag configuration, the gapped area at $\overline{\Gamma}$ is $\sim 0.3\,\mathrm{eV}$ wide (arrow in Fig. 3c), while it is increased to $\sim 0.4\,\mathrm{eV}$ for the Néel configuration (Fig. 3e, within dotted box). For a disordered magnetic structure, we find that features (iv,vi) get shifted upwards by $\sim 100\,\mathrm{meV}$ with respect to the zigzag configuration (Suppl. Fig. S11). Data along the $\overline{\mathrm{K\Gamma K}}$ direction are very similar to the $\overline{\mathrm{M\Gamma M}}$ direction (Suppl. Fig. S9) and, hence, support all our conclusions.

The four bands in the energy region of the observed band shift consist of all Ni 3d and S 3p orbitals as well

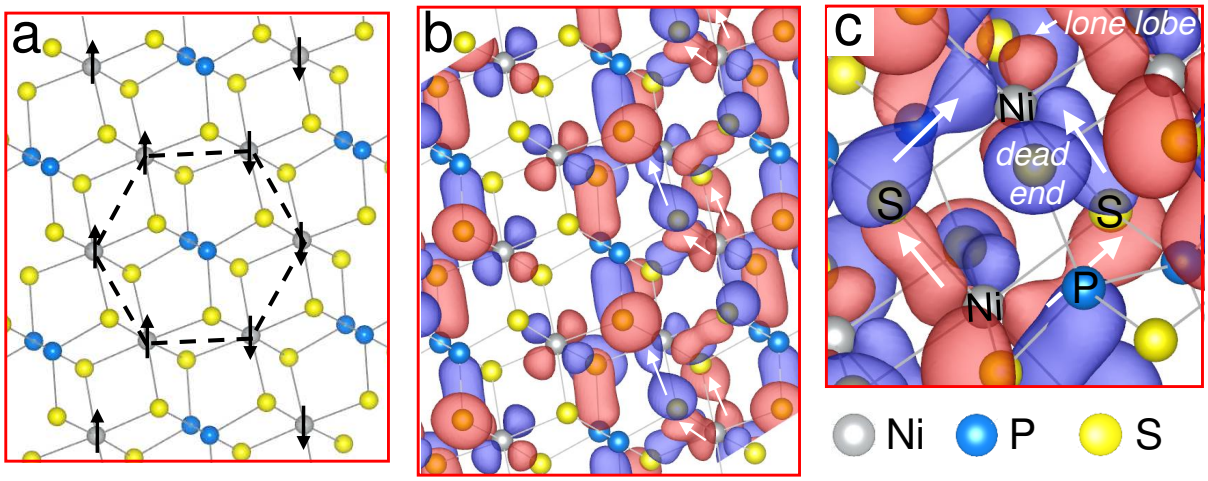

Figure 4. **Charge density of magnetically shifted band.** (a) Crystal structure of a single $NiPS_3$ layer viewed along the c axis (Fig. 1a) with a marked honeycomb of Ni atoms (dashed line) and spin directions in the zigzag AFM configuration (black arrows). (b) Contour planes of the charge density $|\psi(\boldsymbol{x})|^2$ of a state at $E - E_F = -3.9\,\text{eV}$ and $\boldsymbol{k} = \boldsymbol{0}/\text{Å}$ (marked by blue arrow in Fig. 3c). This state likely represents the state that is shifting across T_N. The area and angle of view are the same as in a. Blue and red contour planes mark opposite signs of the wave function. The white arrows highlight the two superexchange paths along Ni $3t_{2g}$-S 3p-S 3p-Ni $3t_{2g}$ between two ferromagnetically coupled Ni atoms. (c) Zoom into b at a tilted angle of view showing the two supexchange paths more clearly (arrows) as well as the lone lobe of the Ni $3t_{2g}$ orbital and the remaining Ni $3t_{2g}$ lobe connected to a S 3p-type dead end orbital (see Suppl. Video). (graphics made by VESTA [1]).

as of a minor contribution from P $3p_z$ (Suppl. section S5). However, only one of these bands features a bonding configuration between neighboring Ni atoms. Figure 4b shows the corresponding charge density for the state at $\overline{\Gamma}$ (charge density of the other three bands, Suppl. section S6). Using the octahedral coordinate system with z along a Ni-S bond, one observes Ni $3t_{2g}$ orbitals (d_{xy}, d_{xz}, d_{yz}) for both Ni zigzag chains, distinct by their spin orientation. On the left chain with spin ↑, the Ni $3t_{2g}$ orbitals do not have any overlap with neighboring orbitals. In contrast, for the right chain, three lobes of each Ni $3t_{2g}$ orbital overlap with a lobe of an adjacent S 3p orbital. The zoom in Fig. 4c as well as rotated views (Suppl. movie) reveal that two of these S 3p orbitals provide a connection path between two Ni atoms (arrows in Fig. 4b), each via the two lobes of a single S 3p orbital. The third connected S 3p orbital (lower lobe of the upper Ni atom in Fig. 4c) is, however, a dead end, i. e. the S 3p orbital does not have any connection to other atoms (Suppl. movie). The final forth lobe of the Ni $3t_{2g}$ orbital is not connected at all and, hence, called a lone lobe as marked in Fig. 4c.

The superexchange path between two Ni atoms by only one S orbital on both sides implies that the interaction is antiferromagnetic. This naturally explains that the band is shifted upwards in energy when these chains become ferromagnetic within the zigzag configuration making the particular bond more unfavorable. It remains unclear why we observe only this change of a band and none of the spin-polarized $3e_g$ levels at higher energy. We conjecture that this is related to the selection rules in our ARPES geometry not being sensitive to the corresponding levels (Suppl. Fig. S6).

We note in passing that we did not find any AFM induced C_3 symmetry breaking in the band structure of $NiPS_3$ by ARPES. The three different $\overline{\Gamma M}$ or $\overline{\Gamma K}$ directions are identical within error bars, albeit the antiferromagnetic zigzag structure breaks the C_3 symmetry (Fig. 1a). Since the DFT+U calculations do not reveal any symmetry breaking that is significantly larger than the energy resolution of the experiment (50 meV), the effect is likely too weak to be detected (Suppl. section S8). In ARPES, we can, moreover, not exclude that the relatively small single domains (1-10 μm) [71] partially overlap within the extraction spot of the photoelectrons (diameter: 5 μm) [72].

This reasonable interpretation leaves us with the question of the origin of the flat feature in ARPES at $E - E_F = -1.3\,\text{eV}$, that is not captured by DFT+U. It appears as a shoulder in the raw ARPES data at energies above the valence band maximum and is nearly identical above and below T_N (Suppl. Fig S12). It, moreover, exhibits the identical photon energy (k_z) dependence as the valence

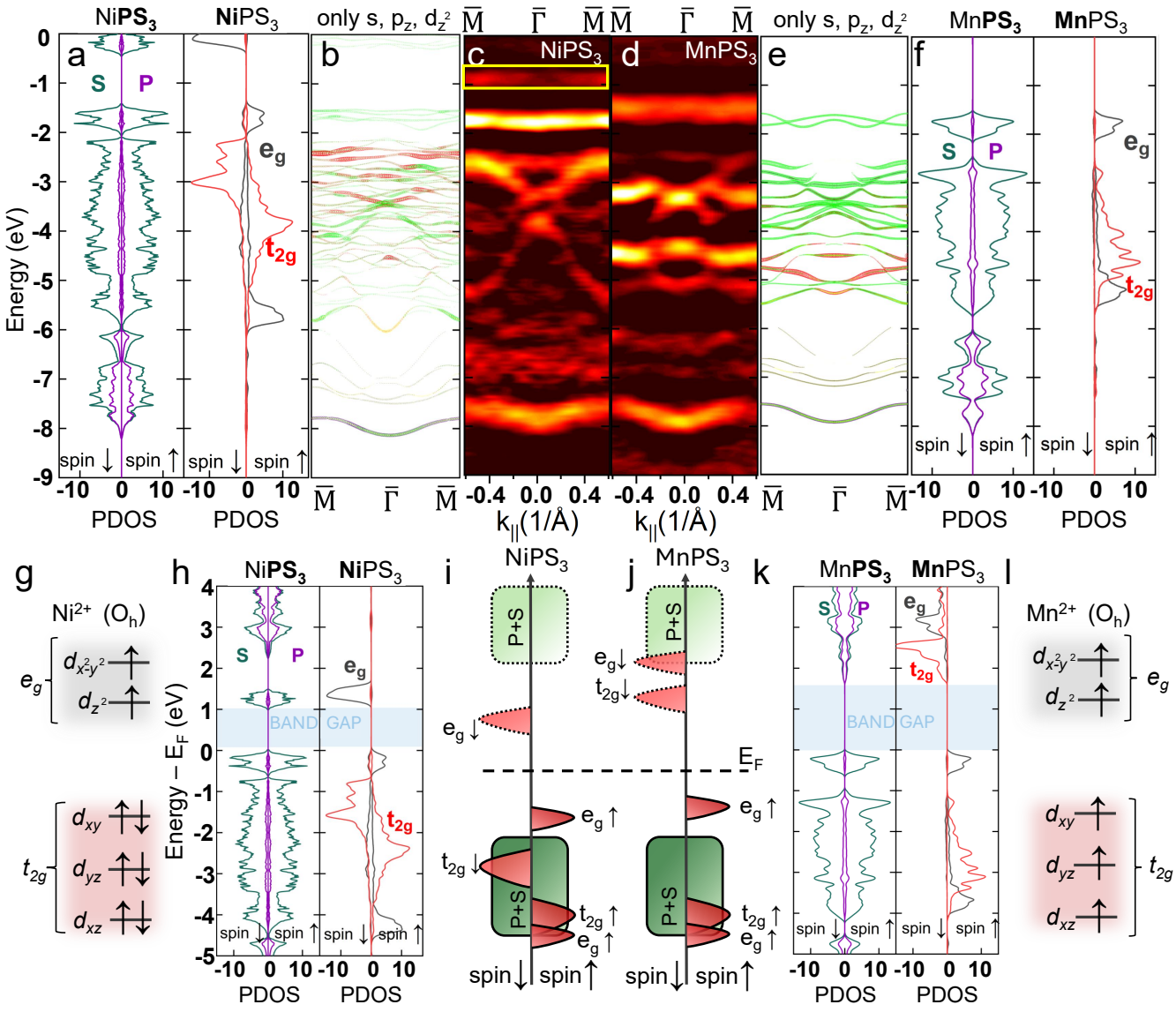

Figure 5. **Comparing $NiPS_3$ and $MnPS_3$ [50].** (a) Spin resolved partial density of states (PDOS) for $NiPS_3$, left: ligand atoms S, P, right: Ni 3d orbitals t_{2g} (d_{xy}, d_{xz}, d_{yz}), e_g ($d_{x^2-y^2}$, d_{z^2}), octahedral coordinate system (see text), DFT+U, $U_{\text{eff}} = 1.6\,\text{eV}$, $k_z = 0.1/\text{Å}$. (b) Band structure corresponding to a after unfolding to the atomic, hexagonal Brillouin zone and selecting the s, p_z and d_{z^2} contributions, z along layer normal (same as Fig. 3c) (c) ARPES curvature of $NiPS_3$, $h\nu = 60\,\text{eV}$, $T = 45\,\text{K}$ (same as Fig. 3d, but shifted upwards by 0.4 eV to match better to $MnPS_3$) (d) same as c for $MnPS_3$ without energy shift, $h\nu = 50\,\text{eV}$, $T = 43\,\text{K}$ ($T_N = 78\,\text{K}$) [50]. (e) same as b for $MnPS_3$, $U_{\text{eff}} = 1.8\,\text{eV}$, $k_z = 0.46/\text{Å}$ [50]. (f) Same as a for $MnPS_3$. (g) Schematic occupation of Ni^{2+} 3d levels in $NiPS_3$. (a)-(c) are adapted to the Fermi level E_F^{Mn} of $MnPS_3$ by a rigid energy shift. (h) Same as a including the conduction band states. (i) Simplified spin polarized PDOS of $NiPS_3$. (j)-(l) Same as g-i for $MnPS_3$ in reverse order.

band maximum (Suppl. Fig. S5, S12). To substantiate its discussion, we compare with the data of $MnPS_3$ [50] (Fig. 5), where all observed features in the ARPES data could be identified with bands of the DFT+U calculation. Figure 5a-f displays the direct comparison using DFT+U data within the respective antiferromagnetic ground state. The figure includes the partial density of states (PDOS) (Fig. 5a,f) where the DOS is projected to the S and P atoms (left) or the e_g ($3d_{z^2,\,x^2-y^2}$) and t_{2g} ($3d_{xy,\,xz,\,yz}$) orbitals of Ni and Mn (right), respectively, using the octahedral coordinates with z along a Ni-S bond. Moreover, the PDOS of minority and majority spins is plotted separately. Finally, the ARPES and DFT+U data of $NiPS_3$ are shifted upwards by 0.4 eV with respect to their $E - E_F$ to align the low energy bands of the two materials. Hence, E_F^{Mn}, the Fermi level of $MnPS_3$, is chosen as reference for for the energy scale.

We find large similarities between $NiPS_3$ and $MnPS_3$. For example, the upper valence band of S 3p/Ni 3d character, respectively S 3p/Mn 3d character is nearly identical in strength of dispersion and orbital contributions. Moreover, the lowest energy bands ($E - E_F^{Mn} < -7.5$ eV) of mixed S 3p/P 3p character are very similar including the relative contribution of S and P orbitals. The energy range in between is, however, different. Firstly, there is a full spin polarization of the t_{2g} orbitals for $MnPS_3$ that is absent for $NiPS_3$. Related, the mixed $3d_{z^2}$/S 3p bands are more confined in energy for $MnPS_3$. In particular, the two bands dominated by Mn $3d_{z^2}$ orbitals ($E - E_F^{Mn} \in [-5, -4]$ eV) are the ones that are most strongly changed across T_N [50]. In contrast, for $NiPS_3$, all bands with $E - E_F^{Mn} \in [-5.5, -2]$ eV have strong, often dominating contributions from Ni 3d orbitals (Suppl. section S5). This difference is in line with the 3d level occupation (see below). Most importantly, the experimental data is very reasonably fitted by DFT+U for both data sets except for the barely dispersing feature at $E - E_F^{Mn} \approx -1$ eV for $NiPS_3$ (highlighted by the yellow box in Fig. 5c). The correspondence between ARPES and DFT+U is also reasonable for $FePS_3$, albeit a stretch of DFT+U data by 7 % was required for a quantitative match [49].

To corroborate that the extra feature (yellow box, Fig. 5c) is not captured by DFT-type calculations, we also performed calculation with other approaches to treat the exchange-correlation energies. We employed HSE while varying the percentage of the Hartree-Fock exchange contribution as well as G_0W_0 and $EVGW_0$ based on a starting PBE band structure (Suppl. section S13). The results feature various shifts of the Ni 3d PDOS, but cannot explain the appearance of an extra feature above the bunch of Ni related bands as observed in ARPES.

Finally, we visualize the expected 3d level occupation for $NiPS_3$ and $MnPS_3$ by using the octahedral coordinates along the bond directions to assign the 3d level orbitals (Fig. 5g-l). For Mn^{2+} $3d^5$, a complete spin polarization of the 3d levels is obtained (Fig. 5k) as expected from Hund's rule (Fig. 5l). In addition, the occupied e_g levels are split into two parts due to the deviations from a perfect octahedral symmetry [73, 74]. On the other hand, Ni^{2+} $3d^8$ shows completely occupied t_{2g} levels, while only the e_g levels are close to fully spin-polarized (Fig. 5h). Hence, the occupation of bands is in line with the expected 3d level occupations and energy splittings. Moreover, for both materials, the bands that are changing most strongly across T_N exhibit significant 3d contributions. This makes us confident that the band assignment by DFT+U is correct and the feature at $E - E_F^{Mn} \approx -1$ eV is beyond the related approximations. It is very likely that 3d level multiplets are involved, maybe including ligand contributions [24], as will be discussed in a separate publication.

III. CONCLUSIONS

We probed the band structure of $NiPS_3$ above and below the Néel temperature using μ-ARPES on flakes exfoliated onto a Au surface. The ARPES data are compared with DFT+U calculations to identify the orbital character of bands. We identify an upwards band shift below T_N by roughly 150 meV for a band close to $\overline{\Gamma}$. This band consists of mixed Ni 3d and S 3p orbitals that likely feature an antiferromagnetic Ni $3t_{2g}$-S 3p-Ni $3t_{2g}$ superexchange path. Beyond the good agreement between DFT+U and ARPES that we also found for $FePS_3$ [49] and $MnPS_3$ [50], we identified a shoulder in the ARPES data above the valence band maximum that could not be attributed to a band of the DFT+U data. This is in striking contrast to $FePS_3$ and $MnPS_3$. We assume that the additional structure is reminiscent of the known strong correlations in $NiPS_3$.

Note added in proof: A very recent publication also shows T-dependent ARPES data of $NiPS_3$ revealing similar band structure features in reasonable correspondance with a similarly selected $U = 2.0$ eV [75].

MATERIALS AND METHODS

$NiPS_3$ crystal growth: Bulk single crystals of $NiPS_3$ were synthesized via the vapor-transport method using stoichiometric amounts of Ni, red P, and S powders, with an additional 5% excess of sulfur to act as a transport agent. The mixture was ground to a fine

powder and then sealed under high vacuum ($\sim 4 \cdot 10^{-5}$ mbar) in a quartz ampoule. This ampoule was then placed in a two-zone furnace, set at 740 °C in the precursor zone and 690 °C in the product zone, for one week.

Sample preparation: We employ an optimized exfoliation method (scotch tape: Nitto ELP BT-150E-KL) to prepare samples with few-layered flakes of $NiPS_3$ in a cleanroom environment. Commercially available Si/SiO_2 (oxide thickness 90 nm) is used as substrate. It has been metal-coated at 370 K with Au (5 nm)/Ti (1 nm) in an ultrahigh vacuum e-beam evaporator. This improves the flake adhesion and renders the substrate conducting, which is necessary to prevent charging during ARPES [50, 59, 76]. A mild O_2 plasma ashing (power = 50 W, flux = 100 sccm) is done at room temperature for 25 s just before exfoliating $NiPS_3$ flakes to efficiently remove organic molecules from the gold surface by oxidation. $NiPS_3$ is exfoliated at 60°C within few minutes after the plasma cleaning. This leads to flakes with diverse thickness, where the desired thickness and flake size are identified using commercial optical and atomic force microscopes [50].

ARPES and XPS experiments: μ-ARPES and XPS were performed at the NanoESCA beamline of the Elettra synchrotron radiation facility in Italy. An ultrahigh vacuum FOCUS NanoESCA photoemission electron microscope (PEEM) was used for the k-space mapping mode operation working at a background pressure of $5 \cdot 10^{-11}$ mbar [77]. To ensure clean surfaces, the samples are firstly annealed at 200°C for a couple of hours prior to ARPES. The synchrotron allows to focus a wide range of photon energies on the sample with a beam spot of 5-10 μm in diameter and total energy resolution (beamline and analyzer) of 50 meV. For our experiments, the photon beam impinged with an incident angle of 65° with respect to the surface normal and with a 5° azimuth relative to the $\overline{\mathrm{M\Gamma M}}$ direction of the crystal. The polarization was within the plane of incidence (p-polarized). The Fermi level has been determined by ARPES on the Au film of the substrate. The sample temperature is adjusted by changing the liquid He flow rate and measured by a Lake Shore DT-670E-BR Si diode placed at the sample holder. So far, only two temperatures are employed for technical reasons such that ARPES data at temperatures closer to T_N have to be postponed to future experiments.

Computational Details: The calculations were performed in the framework of density functional theory (DFT) using the generalized gradient approximation within the PBE flavor [78], as implemented in VASP software [79]. The ion–electron interactions were described by the projector augmented wave (PAW) method [80]. Plane-wave basis cutoff and Γ centered Monkhorst-Pack [81] k-point grid were set to 550 eV and $8 \times 14 \times 8$, respectively. A Gaussian smearing of 0.05 eV was employed for the Brillouin zone (BZ) integration. The interlayer vdW forces were treated within the Grimme scheme using D3 correction [82]. All of the results were obtained using PBE+U method based on Dudarev's approach [83], with the effective on-site Hubbard U parameter ($U_{\mathrm{eff}} = U - J$, where J is fixed to $J = 1$ eV) for the 3d orbitals. The position of the atoms and unit cell were fully optimized within the PBE+U approach. To simulate the disordered paramagnetic state, we used a $4 \times 2 \times 3$ supercell with spin-orbit interaction and randomly set the directions of the magnetic spin moments (in 3D) so that the net moment was zero. Here, we did not optimize the geometric structure, in order to capture only changes in electronic dispersion. Moreover, we used the widely employed band unfolding method to obtain an effective electronic structure [66]. Details on additional calculations given in the Supporting Information are provided in Suppl. Section S13.

ASSOCIATED CONTENT

Data Availability Statement

All data that support the findings of this study are available in zenodo at DOI 10.5281/zenodo.16162323.

Notes

A preprint of this manuscript has been submitted to arXiv [84].

The authors declare no competing financial interest.

SUPPORTING INFORMATION

A possible application of insulating magnetic 2D materials, details on sample preparation, experimental and computational methods, adaption of U_{eff} and k_z including $h\nu$ dependence of ARPES data, individual orbital projections of bands, additional charge density plots, ARPES and DFT band structure along distinct $\overline{K\Gamma K}$ directions, DFT+U band structure of paramagnetic phase, analysis of ARPES structure at $E - E_F = -1.3$ eV, detailed description of the use of ARPES curvature and additional DFT calculations employing HSE and using GW methods.

ACKNOWLEDGEMENT

We acknowledge financial support from the German Research Foundation (DFG) via the project Mo 858/19-1 and Germany's Excellence Strategy Cluster of Excellence: Matter and Light for Quantum Computing(ML4Q) EXC 2004/1 (project Nr. 390534769) from the German Ministry of Education and Research (Project 05K2022 - ioARPES). B.B. acknowledges the support of Humboldt Research Fellowship funded by the Alexander von Humboldt Foundation. M.B. acknowledges financial support from the National Science Centre (NCN), Poland [2024/53/B/ST3/04258]. We gratefully acknowledge Polish high-performance computing infrastructure PLGrid (HPC Center: ACK Cyfronet AGH) for providing computer facilities and support within computational grant no. PLG/2024/017490. K.W. acknowledges support by the National Science Centre in Poland under the project 2024/55/B/ST3/03144. A.K.B. and E.L. were supported by the European Commission via the Marie-Sklodowska Curie action Phonsi (H2020-MSCA-ITN-642656).

REFERENCES

[1] Momma, K.; Izumi, F. *VESTA3* for three-dimensional visualization of crystal, volumetric and morphology data. *J. Appl. Crystal.* **2011**, *44*, 1272–1276.

[2] Kuo, C.-T.; Neumann, M.; Balamurugan, K.; Park, H. J.; Kang, S.; Shiu, H. W.; Kang, J. H.; Hong, B. H.; Han, M.; Noh, T. W.; Park, J.-G. Exfoliation and Raman Spectroscopic Fingerprint of Few-Layer NiPS3 Van der Waals Crystals. *Sci. Rep.* **2016**, *6*, 20904.

[3] Muhammad, Z.; Szpakowski, J.; Abbas, G.; Zu, L.; Islam, R.; Wang, Y.; Wali, F.; Karmakar, A.; Molas, M. R.; Zhang, Y.; Zhu, L.; Zhao, W.; Zhang, H. Anisotropic phonon and magnon vibration and gate-tunable optoelectronic properties of nickel thiophosphite. *2D Mater.* **2023**, *10*, 025001.

[4] Kim, K.; Lim, S. Y.; Lee, J.-U.; Lee, S.; Kim, T. Y.; Park, K.; Jeon, G. S.; Park, C.-H.; Park, J.-G.; Cheong, H. Suppression of magnetic ordering in XXZ-type antiferromagnetic monolayer $NiPS_3$. *Nat. Commun.* **2019**, *10*, 345.

[5] Huang, B.; Clark, G.; Navarro-Moratalla, E.; Klein, D. R.; Cheng, R.; Seyler, K. L.; Zhong, D.; Schmidgall, E.; McGuire, M. A.; Cobden, D. H.; Yao, W.; Xiao, D.; Jarillo-Herrero, P.; Xu, X. Layer-dependent ferromagnetism in a van der Waals crystal down to the monolayer limit. *Nature* **2017**, *546*, 270–273.

[6] Sun, Z. et al. Giant nonreciprocal second-harmonic generation from antiferromagnetic bilayer CrI3. *Nature* **2019**, *572*, 497–501.

[7] Gong, C.; Li, L.; Li, Z.; Ji, H.; Stern, A.; Xia, Y.; Cao, T.; Bao, W.; Wang, C.; Wang, Y.; Qiu, Z. Q.; Cava, R. J.; Louie, S. G.; Xia, J.; Zhang, X. Discovery of intrinsic ferromagnetism in two-dimensional van der Waals crystals. *Nature* **2017**, *546*, 265–269.

[8] Wang, Z. et al. Electric-field control of magnetism in a few-layered van der Waals ferromagnetic semiconductor. *Nat. Nanotechnol.* **2018**, *13*, 554–559.

[9] Deng, Y.; Yu, Y.; Song, Y.; Zhang, J.; Wang, N. Z.; Sun, Z.; Yi, Y.; Wu, Y. Z.; Wu, S.; Zhu, J.; Wang, J.; Chen, X. H.; Zhang, Y. Gate-tunable room-temperature ferromagnetism in two-dimensional Fe3GeTe2. *Nature* **2018**, *563*, 94–99.

[10] Fei, Z.; Huang, B.; Malinowski, P.; Wang, W.; Song, T.; Sanchez, J.; Yao, W.; Xiao, D.; Zhu, X.; May, A. F.; Wu, W.; Cobden, D. H.; Chu, J.-H.; Xu, X. Two-dimensional itinerant ferromagnetism in atomically thin Fe3GeTe2. *Nat. Mater.* **2018**, *17*, 778–782.

[11] Li, H.; Ruan, S.; Zeng, Y. Intrinsic Van Der Waals Magnetic Materials from Bulk to the 2D Limit: New Frontiers of Spintronics. *Adv. Mater.* **2019**, *31*, 1900065.

[12] Zhang, W.; Wong, P. K. J.; Zhu, R.; Wee, A. T. S. Van der Waals magnets: Wonder building blocks for two-dimensional spintronics? *InfoMat* **2019**, *1*, 479–495.

[13] Burch, K. S.; Mandrus, D.; Park, J.-G. Magnetism in two-dimensional van der Waals materials. *Nature* **2018**, *563*, 47–52.

[14] Gong, C.; Zhang, X. Two-dimensional magnetic crystals and emergent heterostructure devices. *Science* **2019**, *363*, 706.

[15] Huang, B.; McGuire, M. A.; May, A. F.; Xiao, D.; Jarillo-Herrero, P.; Xu, X. Emergent phenomena and proximity effects in two-dimensional magnets and heterostructures. *Nat. Mater.* **2020**, *19*, 1276–1289.

[16] Xu, Y.; Ray, A.; Shao, Y.-T.; Jiang, S.; Lee, K.; Weber, D.; Goldberger, J. E.; Watanabe, K.; Taniguchi, T.; Muller, D. A.; Mak, K. F.; Shan, J. Coexisting ferromagnetic–antiferromagnetic state in twisted bilayer CrI3. *Nat. Nanotechnol.* **2021**, *17*, 143–147.

[17] Mi, M.; Zheng, X.; Wang, S.; Zhou, Y.; Yu, L.; Xiao, H.; Song, H.; Shen, B.; Li, F.; Bai, L.; Chen, Y.; Wang, S.; Liu, X.; Wang, Y. Variation between Antiferromagnetism and Ferrimagnetism in NiPS3 by Electron Doping. *Adv. Funct. Mater.* **2022**, *32*, 2112750.

[18] Shin, I. et al. Spin–Orbit Torque Switching in an All-Van der Waals Heterostructure. *Advanced Materials* **2022**, *34*, 2101730.

[19] Ahn, Y.; Guo, X.; Son, S.; Sun, Z.; Zhao, L. Progress and prospects in two-dimensional magnetism of van der Waals materials. *Progr. Quant. Electr.* **2024**, *93*, 100498.

[20] Cham, T. M. J.; Dorrian, R. J.; Zhang, X. S.; Dismukes, A. H.; Chica, D. G.; May, A. F.; Roy, X.; Muller, D. A.; Ralph, D. C.; Luo, Y. K. Exchange Bias Between van der Waals Materials: Tilted Magnetic States and Field-Free Spin–Orbit-Torque Switching. *Advanced Materials* **2024**, *36*, 2305739.

[21] Wang, X.; Cao, J.; Li, H.; Lu, Z.; Cohen, A.; Haldar, A.; Kitadai, H.; Tan, Q.; Burch, K. S.; Smirnov, D.; Xu, W.; Sharifzadeh, S.; Liang, L.; Ling, X. Electronic Raman scattering in the 2D antiferromagnet $NiPS_3$. *Sci. Adv.* **2022**, *8*, eabl7707.

[22] Vaclavkova, D.; Palit, M.; Wyzula, J.; Ghosh, S.; Delhomme, A.; Maity, S.; Kapuscinski, P.; Ghosh, A.; Veis, M.; Grzeszczyk, M.; Faugeras, C.; Orlita, M.; Datta, S.; Potemski, M. Magnon polarons in the van der Waals antiferromagnet FePS3. *Phys. Rev. B* **2021**, *104*, 134437.

[23] Ressouche, E.; Loire, M.; Simonet, V.; Ballou, R.; Stunault, A.; Wildes, A. Magnetoelectric $MnPS_3$ as a candidate for ferrotoroidicity. *Phys. Rev. B* **2010**, *82*, 100408.

[24] Kang, S. et al. Coherent many-body exciton in van der Waals antiferromagnet $NiPS_3$. *Nature* **2020**, *583*, 785–789.

[25] Hwangbo, K.; Zhang, Q.; Jiang, Q.; Wang, Y.; Fonseca, J.; Wang, C.; Diederich, G. M.; Gamelin, D. R.; Xiao, D.; Chu, J.-H.; Yao, W.; Xu, X. Highly anisotropic excitons and multiple phonon bound states in a van der Waals antiferromagnetic insulator. *Nat. Nanotechnol.* **2021**, *16*, 655–660.

[26] Dirnberger, F.; Bushati, R.; Datta, B.; Kumar, A.; MacDonald, A. H.; Baldini, E.; Menon, V. M. Spin-correlated exciton–polaritons in a van der Waals magnet. *Nat. Nanotechnol.* **2022**, *17*, 1060–1064.

[27] Srivastava, P. K.; Hassan, Y.; Ahn, H.; Kang, B.; Jung, S.-G.; Gebredingle, Y.; Joe, M.; Abbas, M. S.; Park, T.; Park, J.-G.; Lee, K.-J.; Lee, C. Exchange Bias Effect in Ferro-/Antiferromagnetic van der Waals Heterostructures. *Nano Lett.* **2020**, *20*, 3978–3985.

[28] Bedoya-Pinto, A.; Ji, J.-R.; Pandeya, A. K.; Gargiani, P.; Valvidares, M.; Sessi, P.; Taylor, J. M.; Radu, F.; Chang, K.; Parkin, S. S. P. Intrinsic 2D-XY ferromagnetism in a van der Waals monolayer. *Science* **2021**, *374*, 616.

[29] Albarakati, S.; Xie, W.-Q.; Tan, C.; Zheng, G.; Algarni, M.; Li, J.; Partridge, J.; Spencer, M. J. S.; Farrar, L.; Xiong, Y.; Tian, M.; Wang, X.; Zhao, Y.-J.; Wang, L. Electric Control of Exchange Bias Effect in $FePS_3/Fe_5GeTe_2$ van der Waals Heterostructures. *Nano Lett.* **2022**, *22*, 6166–6172.

[30] Sun, Z. et al. Dimensionality crossover to a two-dimensional vestigial nematic state from a three-dimensional antiferromagnet in a honeycomb van der Waals magnet. *Nat. Phys.* **2024**, *20*, 1764–1771.

[31] Joy, P. A.; Vasudevan, S. Magnetism in the layered transition-metal thiophosphates MPS_3 (M=Mn, Fe, and Ni). *Phys. Rev. B* **1992**, *46*, 5425–5433.

[32] Wang, F.; Shifa, T. A.; Yu, P.; He, P.; Liu, Y.; Wang, F.; Wang, Z.; Zhan, X.; Lou, X.; Xia, F.; He, J. New Frontiers on van der Waals Layered Metal Phosphorous Trichalcogenides. *Adv. Funct. Mater.* **2018**, *28*, 1802151.

[33] Chittari, B. L.; Park, Y.; Lee, D.; Han, M.; MacDonald, A. H.; Hwang, E.; Jung, J. Electronic and magnetic properties of single-layer MPX_3 metal phosphorous trichalcogenides. *Phys. Rev. B* **2016**, *94*, 184428.

[34] Autieri, C.; Cuono, G.; Noce, C.; Rybak, M.; Kotur, K. M.; Agrapidis, C. E.; Wohlfeld, K.; Birowska, M. Limited Ferromagnetic Interactions in Monolayers of MPS_3 (M = Mn and Ni). *J. Phys. Chem. C* **2022**, *126*, 6791–6802.

[35] Yan, S.; Du, Y.; Zhang, X.; Wan, X.; Wang, D. First-principles study of magnetic interactions and excitations in antiferromagnetic van der Waals material MPX3 (M=Mn, Fe, Co, Ni; X=S, Se). *J. Phys. Condens. Matter* **2023**, *36*, 065502.

[36] Rybak, M.; Faria Junior, P. E.; Woźniak, T.; Scharoch, P.; Fabian, J.; Birowska, M. Magneto-optical anisotropies of two-dimensional antiferromagnetic MPX_3 from first principles. *Phys. Rev. B* **2024**, *109*, 054426.

[37] Sivadas, N.; Daniels, M. W.; Swendsen, R. H.; Okamoto, S.; Xiao, D. Magnetic ground state of semiconducting transition-metal trichalcogenide monolayers. *Phys. Rev. B* **2015**, *91*, 235425.

[38] Kim, S. Y. et al. Charge-Spin Correlation in van der Waals Antiferromagnet NiPS3. *Phys. Rev. Lett.* **2018**, *120*, 136402.

[39] Lane, C.; Zhu, J.-X. Thickness dependence of electronic structure and optical properties of a correlated van der Waals antiferromagnetic NiPS3 thin film. *Phys. Rev. B* **2020**, *102*, 075124.

[40] Wang, X.; Cao, J.; Lu, Z.; Cohen, A.; Kitadai, H.; Li, T.; Tan, Q.; Wilson, M.; Lui, C. H.; Smirnov, D.; Sharifzadeh, S.; Ling, X. Spin-induced linear polarization of photoluminescence in antiferromagnetic van der Waals crystals. *Nat. Mater.* **2021**, *20*, 964–970.

[41] Jana, D.; Kapuscinski, P.; Mohelsky, I.; Vaclavkova, D.; Breslavetz, I.; Orlita, M.; Faugeras, C.; Potemski, M. Magnon gap excitations and spin-entangled optical transition in the van der Waals antiferromagnet $NiPS_3$. *Phys. Rev. B* **2023**, *108*, 115149.

[42] Klaproth, T.; Aswartham, S.; Shemerliuk, Y.; Selter, S.; Janson, O.; van den Brink, J.; Büchner, B.; Knupfer, M.; Pazek, S.; Mikhailova, D.; Efimenko, A.; Hayn, R.; Savoyant, A.; Gubanov, V.; Koitzsch, A. Origin of the Magnetic Exciton in the van der Waals Antiferromagnet NiPS3. *Phys. Rev. Lett.* **2023**, *131*, 256504.

[43] Song, F.; Lv, Y.; Sun, Y.-J.; Pang, S.; Chang, H.; Guan, S.; Lai, J.-M.; Wang, X.-J.; Wu, B.; Hu, C.; Yuan, Z.; Zhang, J. Manipulation of anisotropic Zhang-Rice exciton in NiPS3 by magnetic field. *Nat. Commun.* **2024**, *15*, 7841.

[44] Wang, X.; Tan, Q.; Li, T.; Lu, Z.; Cao, J.; Ge, Y.; Zhao, L.; Tang, J.; Kitadai, H.; Guo, M.; Li, Y.-M.; Xu, W.; Cheng, R.; Smirnov, D.; Ling, X. Unveiling the spin evolution in van der Waals antiferromagnets via magneto-exciton effects. *Nat. Commun.* **2024**, *15*, 8011.

[45] Allington, C. J.; Belvin, C. A.; Seifert, U. F.; Ye, M.; Tai, T.; Baldini, E.; Son, S.; Kim, J.; Park, J.; Park, J.-G.; Balents, L.; Gedik, N. Distinct Optical Excitation Mechanisms of a Coherent Magnon in a van der Waals Antiferromagnet. *Phys. Rev. Lett.* **2025**, *134*, 066903.

[46] Du, K.-Z.; Wang, X.-Z.; Liu, Y.; Hu, P.; Utama, M. I. B.; Gan, C. K.; Xiong, Q.; Kloc, C. Weak Van der Waals Stacking, Wide-Range Band Gap, and Raman Study on Ultrathin Layers of Metal Phosphorus Trichalcogenides. *ACS Nano* **2016**, *10*, 1738–1743.

[47] Scheie, A.; Park, P.; Villanova, J. W.; Granroth, G. E.; Sarkis, C. L.; Zhang, H.; Stone, M. B.; Park, J.-G.; Okamoto, S.; Berlijn, T.; Tennant, D. A. Spin wave Hamiltonian and anomalous scattering in NiPS3. *Phys. Rev. B* **2023**, *108*, 104402.

[48] Wildes, A. R.; Simonet, V.; Ressouche, E.; McIntyre, G. J.; Avdeev, M.; Suard, E.; Kimber, S. A. J.; Lançon, D.; Pepe, G.; Moubaraki, B.; Hicks, T. J. Magnetic structure of the quasi-two-dimensional antiferromagnetNiPS3. *Phys. Rev. B* **2015**, *92*, 224408.

[49] Pestka, B. et al. Identifying Band Structure Changes of FePS3 across the Antiferromagnetic Phase Transition. *ACS Nano* **2024**, *18*, 32924.

[50] Strasdas, J. et al. Electronic Band Structure Changes across the Antiferromagnetic Phase Transition of Exfoliated $MnPS_3$ Flakes Probed by μ-ARPES. *Nano Lett.* **2023**, *23*, 10342.

[51] Afanasiev, D.; Hortensius, J. R.; Matthiesen, M.; Mañas-Valero, S.; Šiškins, M.; Lee, M.; Lesne, E.; van der Zant, H. S. J.; Steeneken, P. G.; Ivanov, B. A.; Coronado, E.; Caviglia, A. D. Controlling the anisotropy of a van der Waals antiferromagnet with light. *Sci. Adv.* **2021**, *7*, abf3096.

[52] Basnet, R.; Wegner, A.; Pandey, K.; Storment, S.; Hu, J. Highly sensitive spin-flop transition in antiferromagnetic van der Waals material MPS_3 (M=Ni and Mn). *Phys. Rev. Mat.* **2021**, *5*, 064413.

[53] Basnet, R.; Kotur, K. M.; Rybak, M.; Stephenson, C.; Bishop, S.; Autieri, C.; Birowska, M.; Hu, J. Controlling magnetic exchange and anisotropy by nonmagnetic ligand substitution in layered MPX_3 (M = Ni, Mn; X = S, Se). *Phys. Rev. Research* **2022**, *4*, 023256.

[54] Yan, M.; Jin, Y.; Voloshina, E.; Dedkov, Y. Electronic Correlations in FexNiyPS3 Van der Waals Materials: Insights from Angle-Resolved Photoelectron Spectroscopy and DFT. *J. Phys. Chem. Lett.* **2023**, *14*, 9774—-9779.

[55] Nitschke, J. E.; Bhumla, P.; Willershausen, T.; Merisescu, P.; Janas, D.; Sternemann, L.; Gutnikov, M.; Schiller, K.; Mischke, V.; Capra, M.; Arndt, M. S.; Botti, S.; Cinchetti, M. Electronic structure reorganization in MPS_3 via d-shell-selective alkali metal doping. *arXiv:* **2025**, 2506.01527.

[56] Bianchi, M.; Acharya, S.; Dirnberger, F.; Klein, J.; Pashov, D.; Mosina, K.; Sofer, Z.; Rudenko, A. N.; Katsnelson, M. I.; van Schilfgaarde, M.; Rösner, M.; Hofmann, P. Paramagnetic electronic structure of CrSBr: Comparison between ab initio GW theory and angle-resolved photoemission spectroscopy. *Phys. Rev. B* **2023**, *107*, 235107.

[57] De Vita, A. et al. Influence of Orbital Character on the Ground State Electronic Properties in the van Der Waals Transition Metal Iodides VI3 and CrI3. *Nano Lett.* **2022**, *22*, 7034—-7041.

[58] Nitschke, J. E.; Esteras, D. L.; Gutnikov, M.; Schiller, K.; Mañas-Valero, S.; Coronado, E.; Stupar, M.; Zamborlini, G.; Ponzoni, S.; Baldoví, J. J.; Cinchetti, M. Valence band electronic structure of the van der Waals antiferromagnet FePS3. *Mater. Today Electron.* **2023**, *6*, 100061.

[59] Koitzsch, A.; Klaproth, T.; Selter, S.; Shemerliuk, Y.; Aswartham, S.; Janson, O.; Büchner, B.; Knupfer, M. Intertwined electronic and magnetic structure of the van-der-Waals antiferromagnet Fe2P2S6. *npj Quantum Mater.* **2023**, *8*, 27.

[60] Voloshina, E.; Jin, Y.; Dedkov, Y. ARPES studies of the ground state electronic properties of the van der Waals transition metal trichalcogenide $CoPS_3$. *Chem. Phys. Lett.* **2023**, *823*, 140511.

[61] Yan, M.; Jin, Y.; Wu, Z.; Tsaturyan, A.; Makarova, A.; Smirnov, D.; Voloshina, E.; Dedkov, Y. Correlations in the Electronic Structure of van der Waals NiPS3 Crystals: An X-ray Absorption and Resonant Photoelectron Spectroscopy Study. *J. Phys. Chem. Lett.* **2021**, *12*, 2400––2405.

[62] Currò, G. M.; Grasso, V.; Neri, F.; Silipigni, L. The effects of the lithium intercalation on the X-ray photoelectron spectra of NiPS3. *Il Nuovo Cimento D* **1995**, *17*, 37–52.

[63] Piacentini, M.; Khumalo, F.; Olson, C.; Anderegg, J.; Lynch, D. Optical transitions, XPS, electronic states in NiPS3. *Chem. Phys.* **1982**, *65*, 289—304.

[64] Coad, J.; Rivière, J. Origin of fine structure in the Auger spectrum of sulphur on a nickel surface. *Proceedings of the Royal Society of London. A. Mathematical and Physical Sciences* **1972**, *331*, 403—415.

[65] Justin Gorham NIST X-ray Photoelectron Spectroscopy Database - SRD 20. 2012; `https://srdata.nist.gov/xps/`.

[66] Popescu, V.; Zunger, A. Extracting E versus k effective band structure from supercell calculations on alloys and impurities. *Phys. Rev. B* **2012**, *85*, 085201.

[67] Moser, S. An experimentalist's guide to the matrix element in angle resolved photoemission. *J. Electr. Spectr. Rel. Phen.* **2017**, *214*, 29–52.

[68] Wang, Y.-M.; Zhang, J.-F.; Li, C.-H.; Ma, X.-L.; Ji, J.-T.; Jin, F.; Lei, H.-C.; Liu, K.; Zhang, W.-L.; Zhang, Q.-M. Raman scattering study of magnetic layered MPS3 crystals (M = Mn, Fe, Ni)*. *Chin. Phys. B* **2019**, *28*, 056301.

[69] Fano, U. Effects of Configuration Interaction on Intensities and Phase Shifts. *Phys. Rev.* **1961**, *124*, 1866.

[70] Hüfner, S. *Photoelectron Spectroscopy: Principles and Applications*; Advanced Texts in Physics; Springer Berlin Heidelberg, 2013.

[71] Lee, Y.; Kim, C.; Son, S.; Cui, J.; Park, G.; Zhang, K.-X.; Oh, S.; Cheong, H.; Kleibert, A.; Park, J.-G. Imaging Thermally Fluctuating Néel Vectors in van der Waals Antiferromagnet NiPS3. *Nano Lett.* **2024**, *24*, 6043.

[72] He, W.; Shen, Y.; Wohlfeld, K.; Sears, J.; Li, J.; Pelliciari, J.; Walicki, M.; Johnston, S.; Baldini, E.; Bisogni, V.; Mitrano, M.; Dean, M. P. M. Magnetically

propagating Hund's exciton in van der Waals antiferromagnet NiPS3. *Nat. Commun.* **2024**, *15*, 3496.

[73] Figgis, B. N.; Hitchman, M. A. *Ligand Field Theory and Its Applications*; Wiley–VCH, 2000.

[74] Trimarchi, G.; Wang, Z.; Zunger, A. Polymorphous band structure model of gapping in the antiferromagnetic and paramagnetic phases of the Mott insulators MnO, FeO, CoO, and NiO. *Phys. Rev. B* **2018**, *97*, 035107.

[75] Cao, Y. et al. Revealing the electronic structure of van der Waals antiferromagnetic $NiPS_3$ through synchrotron-based μ-ARPES and alkali metal dosing. *Phys. Rev. Mater.* **2025**, *9*.

[76] Velický, M. et al. Mechanism of Gold-Assisted Exfoliation of Centimeter-Sized Transition-Metal Dichalcogenide Monolayers. *ACS Nano* **2018**, *12*, 10463–10472, PMID: 30265515.

[77] Schneider, C.; Wiemann, C.; Patt, M.; Feyer, V.; Plucinski, L.; Krug, I.; Escher, M.; Weber, N.; Merkel, M.; Renault, O.; Barrett, N. Expanding the view into complex material systems: From micro-ARPES to nanoscale HAXPES. *J. Electr. Spectr. Rel. Phenom.* **2012**, *185*, 330–339.

[78] Perdew, J. P.; Burke, K.; Ernzerhof, M. Generalized Gradient Approximation Made Simple. *Phys. Rev. Lett.* **1996**, *77*, 3865–3868.

[79] Kresse, G.; Müller, J. F. Efficiency of ab-initio total energy calculations for metals and semiconductors using a plane-wave basis set. *Comp. Mater. Sci.* **1996**, *6*, 15 – 50.

[80] Holzwarth, N. A. W.; Tackett, A. R.; Matthews, G. E. A Projector Augmented Wave (PAW) code for electronic structure calculations, Part I: atom paw for generating atom-centered functions. *Comput. Phys. Comm.* **2001**, *135*.

[81] Monkhorst, H. J.; Pack, J. D. Special points for Brillouin-zone integrations. *Phys. Rev. B* **1976**, *13*, 5188–5192.

[82] Grimme, S.; Antony, J.; Ehrlich, S.; Krieg, H. A consistent and accurate ab initio parametrization of density functional dispersion correction (DFT-D) for the 94 elements H-Pu. *J. Chem. Phys.* **2010**, *132*, 154104.

[83] Dudarev, S. L.; Botton, G. A.; Savrasov, S. Y.; Humphreys, C. J.; Sutton, A. P. Electron-energy-loss spectra and the structural stability of nickel oxide: An LSDA+U study. *Phys. Rev. B* **1998**, *57*, 1505–1509.

[84] Pestka, B. et al. Probing the band structure of the strongly correlated antiferromagnet NiPS3 across its phase transition. *arXiv:* **2025**, 2507.14890.

Supplementary Information: Probing the band structure of the strongly correlated antiferromagnet $NiPS_3$ across its phase transition

Benjamin Pestka[†],[1] Biplab Bhattacharyya[†],[1] Miłosz Rybak[†],[2] Jeff Strasdas,[1] Adam K. Budniak,[3] Adi Harchol,[3] Marcus Liebmann,[1] Niklas Leuth,[1] Honey Boban,[4] Vitaliy Feyer,[4] Iulia Cojocariu,[4,5,6] Daniel Baranowski,[4,7] Simone Mearini,[4] Lutz Waldecker,[8] Bernd Beschoten,[8] Christoph Stampfer,[8] Yaron Amouyal,[9] Lukasz Plucinski,[4] Efrat Lifshitz,[3] Krzysztof Wohlfeld,[10] Magdalena Birowska,[10] and Markus Morgenstern[*1]

[1] *II. Institute of Physics B and JARA-FIT, RWTH-Aachen University, 52074 Aachen, Germany*
[2] *Department of Semiconductor Materials Engineering Faculty of Fundamental Problems of Technology Wrocław University of Science and Technology Wybrzeże Wyspiańskiego 27, 50-370 Wrocław, Poland*
[3] *Schulich Faculty of Chemistry, Solid State Institute, Russell Berrie Nanotechnology Institute, Technion, Haifa 3200003, Israel*
[4] *Forschungszentrum Jülich, Peter Grünberg Institute (PGI-6), 52425 Jülich, Germany*
[5] *Physics Department, University of Trieste, Trieste, 34127 Italy*
[6] *Elettra – Sincrotrone Trieste S.C.p.A., S.S. 14 km 163.5, Trieste, 34149 Italy*
[7] *Physical and Computational Sciences, Directorate and Institute for Integrated Catalysis, Pacific Northwest National Laboratory, Richland, WA 99354, USA*
[8] *2nd Institute of Physics and JARA-FIT, RWTH-Aachen University, Aachen 52074, Germany*
[9] *Department of Materials Science and Engineering, Technion – Israel Institute of Technology, Haifa 3200003, Israel*
[10] *Institute of Theoretical Physics, Faculty of Physics, Universityof Warsaw, Pasteura St. 5, 02-093 Warsaw, Poland*

(Dated: January 6, 2026)

[†]These authors contributed equally to this work.
[*]Corresponding author: M. Morgenstern, Email: mmorgens@physik.rwth-aachen.de

CONTENTS

S1. POSSIBLE ELECTRON-MAGNON TRANSDUCER

The strong exciton–magnon coupling in van der Waals magnets as $NiPS_3$ offers novel opportunities for opto-magnetic applications, e. g. towards transducers between magnons and photons in the infrared range. It has been shown that magnons can be tracked coherently in 2D materials, e. g. in CrSBr, by time-resolved shifts of their exciton energy by $\Delta E \sim 20\,\text{meV}$ down to ps time scales [1]. More recently, pump–probe spectroscopy on $NiPS_3$ revealed ultrafast reflectivity changes that are related to spin dynamics via the critical slowing down around T_N [2]. On the other hand, magnons as information carriers have been intensely pursued, meanwhile leading to rather complex devices as, e. g., spin-wave multiplexers [3–5]. Thus,

magnon–exciton coupling, in which Coulomb-bound electron–hole pairs interact with the collective spin excitations, could enable transducers between spin information and optical channels or vice versa. Therefor, the magnon properties of the 2D materials can be imprinted coherently in the optical intensity as already demonstrated [1, 6], or into the light polarization since the exciton's dipole moment of, e. g. $NiPS_3$ is locked to the local spin orientation [7]. Moreover, the exciton-magnon interaction in 2D materials is tunable via strain or interface design, shifting magnon frequencies or adjusting coupling strengths [6]. This is favorable for tunable or selective transducers. Finally, $NiPS_3$ has a relatively large fundamental magnon gap of 5.3 meV with narrow linewidth (0.1 meV) as probed by THz absorption [8]. This points towards low noise magnonic operation. The transfer of the magnons, e g. to $Y_3Fe_5O_12$ (YIG) still has to be explored, but is possible in principle [9]. Such an approach towards efficient magnon-photon transducers in the infrared would combine the low-dissipation propagation of magnons with the coherent long-range communication by photons via fibers, eventually enabling more scalable, magnonic technologies. Of course, the relatively efficient spin-optical interface might also be used for other interconnects between spin-based devices.

S2. ADJUSTING THE BRILLOUIN ZONE TO THE ARPES DATA

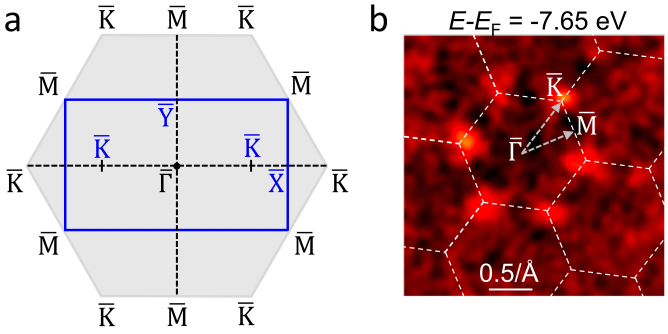

Figure S1. **Brillouin zone (BZ)** (a) Two-dimensional projections of the BZ to the surface for the atomic arrangement of $NiPS_3$ without magnetism (grey hexagon) and for the zigzag-type AFM arrangement (blue rectangle), high symmetry points are marked. (b) (k_x, k_y) plot of ARPES curvature intensity, E-E_F = -7.65 eV, $h\nu$ = 60 eV, T = 45 K, the hexagonal surface projection of the atomic BZs is overlaid (dashed white lines), arrows: $\overline{\Gamma M}$, $\overline{\Gamma K}$ direction.

Figure S1a displays the Brillouin zone projection to the surface (Fig. S5a) for the atomic arrangement without magnetism (grey hexagon) and with the antiferromagnetic (AFM) zig-zag structure (blue rectangle). The $\overline{K}$ points are backfolded to the interior of the magnetic BZ, while the $\overline{M}$ points are either not affected (four times) or backfolded to $\overline{\Gamma}$ (two times). In the main text, we consistently used the atomic, hexagonal Brillouin zone for labeling and we unfolded to this Brillouin zone for the DFT+U data [10]. To adjust the BZ orientation to the angular dependence of the photoelectron intensity, we employ (k_x, k_y) plots at energies where bands exhibit maxima at the BZ boundary. For feature ix of the band structure (mixed P/S band, Fig. S3a,d), this reveals a hexagonal symmetry (Fig. S1b) that can be adapted to the surface projection of the atomic BZ (dashed hexagons). This symmetry is visible above and below T_N showing that the ARPES data of this band are not affected by the magnetically induced backfolding. We checked that this is true for all energies where the hexagonal symmetry is clearly apparent, including bands that involve Ni 3d orbitals. Hence, the AFM superstructure does not change the periodicity of the wave functions significantly as also evidenced by the unfolding procedure (Fig. S2). The overlay of the hexagon edges of the projected BZ to the maxima in the (k_x, k_y) plot reveals straightforwardly the orientation of the BZ and the relation between photoemission angle and the value of $k_{\parallel}$ by relating to values from the literature ($\overline{\Gamma M}$: 0.62/Å, $\overline{\Gamma K}$: 0.72/Å [12, 13]).

Figure S2 displays the comparison between the calculated initial states in the magnetic, rectangular Brillouin zone and the unfolded data (hexagonal Brillouin zone), once for all bands (Fig. S2a-b) and once for only the bands with more than 10 % contribution of s, p_z and d_{z^2} orbitals (Fig. S2c-d). We choose a $\overline{M\Gamma M}$ direction that is unchanged by the AFM order (green double arrow in the Brillouin zone at the upper left) to ease the comparison. Multiple bands are simply backfolded by the AFM periodicity and disappear by unfolding. Importantly, this reduces the relevant bands for comparison to the ARPES data significantly besides the reduction to orbital contributions given by the matrix element projection to final state plane waves as for our electric field geometry of the incident photon beam [11, 14].

S3. ADAPTING U_{eff} OF DFT+U CALCULATIONS TO ARPES DATA

In order to assign orbital characters to the bands visible in ARPES, one has to select the best matching on-site energy U_{eff} of the DFT+U calculations as well as the best

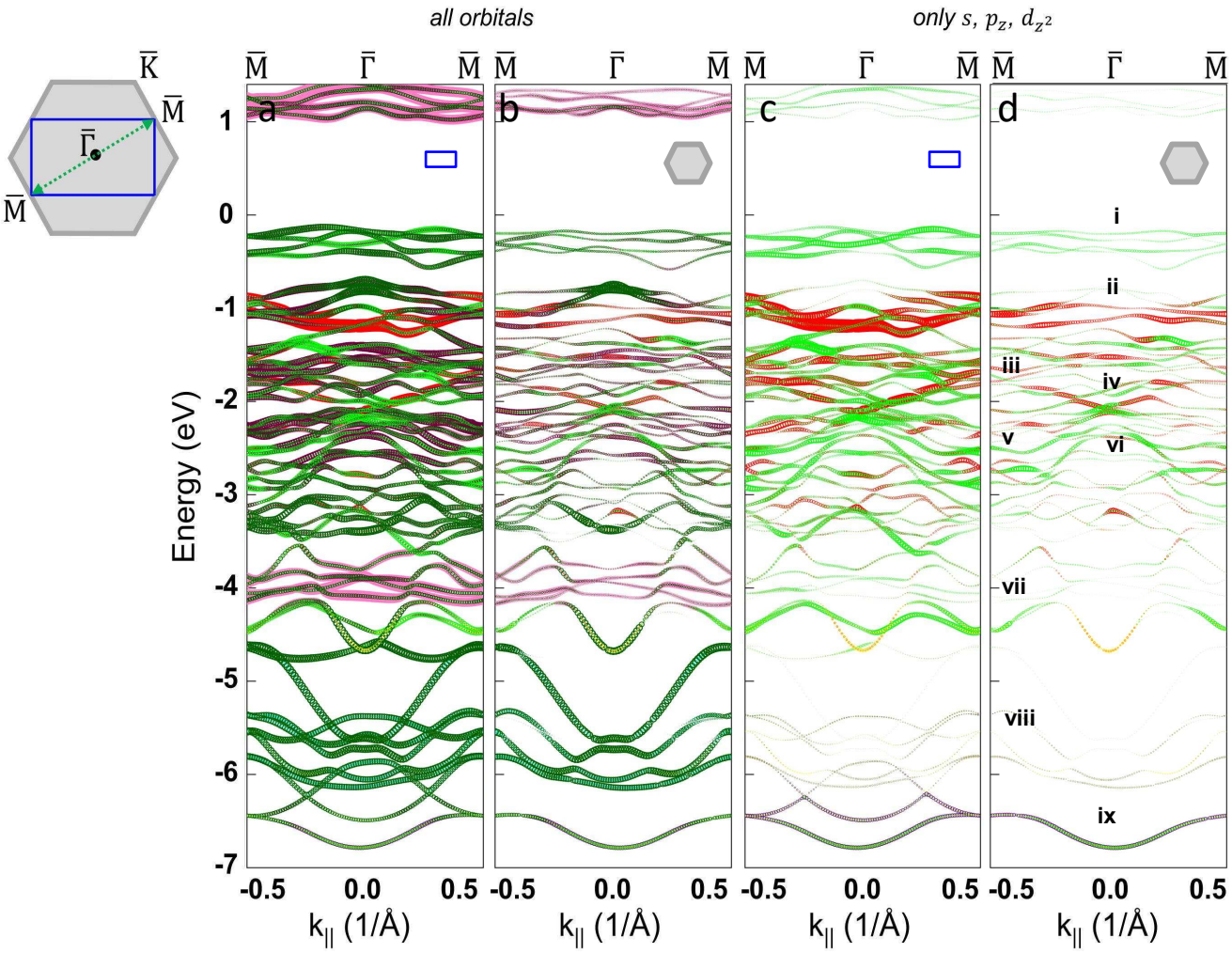

Figure S2. **Comparing folded and unfolded DFT+U data.** (a) DFT+U band structure displayed in the magnetic Brillouin zone (blue rectangle) with all bands, $U_{\text{eff}} = 1.6\,\text{eV}$, $k_z = 0.1/\text{Å}$, symbol diameter is proportional to the percentage of the orbital contribution to this state, color code as in Fig. 3, main text. (b) Same as a after unfolding the bands to the hexagonal atomic BZ (gray hexagon) [10]. (c), (d) Same as a and b, but depicting only the selected orbitals as marked on top according to simplified selection rules [11].

matching wave number k_z perpendicular to the surface. For that purpose, we employ several pronounced features of the ARPES data and recursively compare them with the DFT+U band structure for different U_{eff} and k_z. We eventually selected $U_{\text{eff}} = 1.6\,\text{eV}$ and $k_z = 0.1/\text{Å}$ as described in detail in the next sections. This selection does not lead to a one-to-one correspondence between ARPES and DFT+U data, but it gives a solid understanding of the orbital development of the bands with these parameters and, hence, of its robustness. In Fig. 3, main text, the most important features in ARPES are already labeled as i-ix. For comparison of these features with DFT+U band structures, we only use the bands with a strong s, p_z or d_{z^2} character according to the simplified selection rules in our photon beam geometry as discussed in the main text [11] and the unfolded band structure.

Figure S3 shows the comparison of ARPES curvature data, recorded at $h\nu = 60\,\text{eV}$, with DFT+U data at various U_{eff} and optimized $k_z = 0.1/\text{Å}$. The lowest energy band (feature ix) that is nearly parabolic at $\overline{\Gamma}$ and consists of S 3p and P 3p contributions (Fig. S6) barely shifts with energy due to its missing Fe 3d orbitals. We use it to

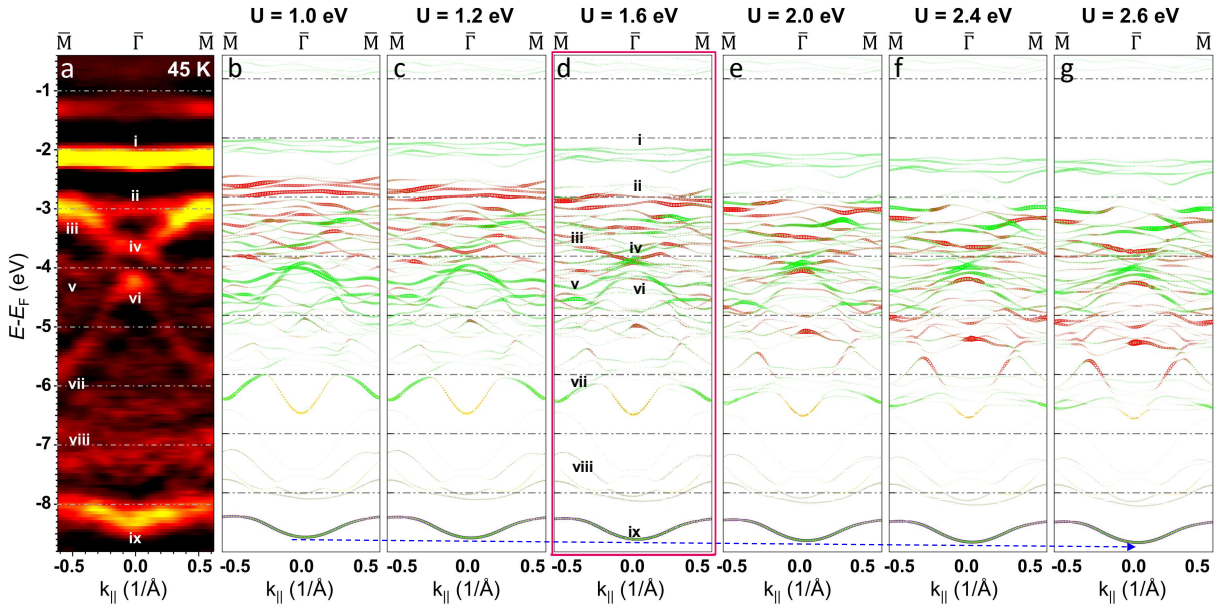

Figure S3. **Adapting the U_{eff} parameter.** (a) ARPES curvature plot, $h\nu = 60\,\text{eV}$, $T = 45\,\text{K}$, $\overline{\text{M}\Gamma\text{M}}$ direction, same color scale as in Fig. 3, main text. (b)-(g) DFT+U band structure at various U_{eff} as marked for selected orbitals with s, p_z and d_{z^2} character, symbol diameter is proportional to the percentage of the orbital contribution to this state, color code as in Fig. 3, main text, $k_z = 0.1/\text{Å}$. Labels i-ix and dashed blue arrow are used to compare theory with experiment as discussed in the text. The red box highlights the selected $U_{\text{eff}} = 1.6\,\text{eV}$.

rigidly shift the energy scale of the DFT+U data to the ARPES data given with respect to E_{F}. The band from DFT+U is chosen slightly below the band in ARPES for reasons described latter. The rigid shift implies a slight n-doping of the material regarding the known energy gap of 1.8 eV in $NiPS_3$ [15]. This is visible as faint bands at the top of the calculated band structures belonging to the conduction band.

For U_{eff} selection, we use bands that are changing with U_{eff}. The topmost flat green bands (feature i) of dominating S 3p character with contributions from Ni $3d_{xz,yz}$ (Fig. S6) move downwards with increasing U_{eff} matching the experiment at $U_{\text{eff}} = 1.6 - 2.0\,\text{eV}$. Feature ii is a relatively flat band in ARPES identified with the flat DFT+U band of dominating Fe $3d_{z^2}$ character. It also moves downwards with energy matching best at $U_{\text{eff}} = 2.0\,\text{eV}$, where also the gap between features i and ii matches the experiment. The small gap at $\overline{\Gamma}$ between features iv and vi appears reminiscent to a gap opening at a former crossing point in the experiment. This gap is most pronounced at $U_{\text{eff}} = 1.0 - 1.2\,\text{eV}$ in DFT +U being more faint at $U_{\text{eff}} = 1.6\,\text{eV}$ and matches best to the experiment at $U_{\text{eff}} = 1.2\,\text{eV}$. The bands surrounding the crossing point at $\overline{\Gamma}$ get, moreover, significantly more flat than in the experiment for $U_{\text{eff}} > 1.6\,\text{eV}$. Recall that this is the area of band change across T_{N} (Fig. 2, main text). The steep band between features vi and vii is not found continuous in energy for any U_{eff}, but exhibits a reasonably similar slope as in the ARPES data around vii for $U_{\text{eff}} = 1.0\,\text{eV}$ with continuously decreasing slope for higher U_{eff}. Feature viii, finally, is too weak in experiment and calculations to be used for U_{eff} selection.

Summarizing, $U_{\text{eff}} = 1.6\,\text{eV}$ is the best compromise between the slightly larger U_{eff} required for the high energy bands and the slightly lower U_{eff} necessary to describe the lower energy bands.

S4. ADAPTING k_z OF DFT+U CALCULATIONS TO ARPES

We followed a similarly detailed comparison as described in Supplementary Section S3 for matching k_z. Figure S4 depicts the ARPES data and the DFT+U data

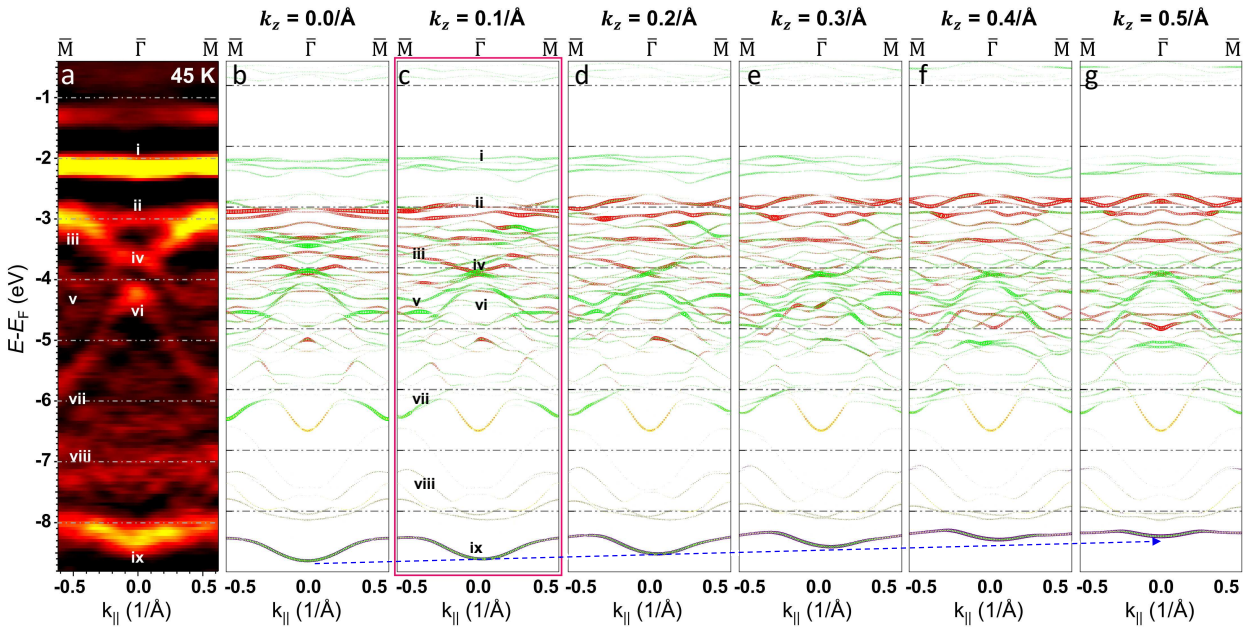

Figure S4. **Adapting k_z parameter.** (a) ARPES curvature plot, $h\nu = 60\,\mathrm{eV}$, $T = 45\,\mathrm{K}$, $\overline{\mathrm{M\Gamma M}}$ direction, same color scale as in Fig. 3, main text. (b)–(g) DFT+U band structures at various k_z as marked, $U_{\mathrm{eff}} = 1.6\,\mathrm{eV}$, only bands with significant s, p_z and d_{z^2} character are displayed [11], symbol diameter is proportional to the percentage of the orbital contribution to this state, color code as in Fig. 3, main text. Labels i-ix and dashed blue arrow are used for comparison to ARPES as discussed in the text. The red box highlights the selected $k_z = 0.1/\mathrm{Å}$.

at $U_{\mathrm{eff}} = 1.6\,\mathrm{eV}$ for various k_z highlighting the eventually selected $k_z = 0.1/\mathrm{Å}$. One has to keep in mind that k_z is changing for constant $h\nu$ with $E - E_{\mathrm{F}}$ by roughly $0.25/\mathrm{Å}$ across the energy range displayed in Fig. S4a (see below) with the largest k_z at the top.

We start with features i and ix, which move downwards and upwards, respectively, with increasing k_z. The best match of their energy distance to the ARPES data is at $k_z \approx 0.3/\mathrm{Å}$. Next, the gap between features i and ii gets smaller with increasing k_z and matches best to the ARPES data at $k_z = 0.0 - 0.2/\mathrm{Å}$. Moreover, the wing-like features consisting of iii, iv and v change in shape with k_z exhibiting a reasonable match at $k_z = 0.1/\mathrm{Å}$. This is also true for the steepness of the bands around feature vi that are less steep at higher and lower k_z than $k_z = 0.1/\mathrm{Å}$. Finally, the suppressed curvature between features ii and iv might be related to the only weakly appearing bands at $k_z \geq 0.1/\mathrm{Å}$ in that energy range, where bands are stronger at $k_z = 0.0/\mathrm{Å}$. Hence, with a certain ambiguity, we choose $k_z = 0.1/\mathrm{Å}$ as the best compromise.

Using the k_z selection for $h\nu = 60\,\mathrm{eV}$, we can relate different photon energies to different k_z. We use the simplified free electron model for final states in the crystal with origin of the corresponding free electron parabola at V_0 [16]. Hence, the final state energy E_{final} at wavevector $\boldsymbol{k}$ inside the crystal reads:

$$E_{\mathrm{final}}(\boldsymbol{k}) = \frac{\hbar^2 \boldsymbol{k}^2}{2m} - V_0. \tag{1}$$

The kinetic electron energy in vacuum reads:

$$E_{\mathrm{kin}}^{\mathrm{vac}} = E_{\mathrm{kin}}^{\mathrm{A}} - \phi + \phi^{\mathrm{A}} \tag{2}$$

with the work function of the $NiPS_3$ flake $\phi = 5.375\,\mathrm{eV}$, the work function of the analyzer $\phi^{\mathrm{A}} = 4.6\,\mathrm{eV}$, and the kinetic energy $E_{\mathrm{kin}}^{\mathrm{A}}$ of the photoelectrons at the analyzer. ϕ^{A} was determined using $E_{\mathrm{kin}}^{\mathrm{A}}$ of photoelectrons emitted from the Fermi level E_{F} measured on the gold substrate next to a $NiPS_3$ flake. ϕ is determined on a $NiPS_3$ flake from the onset energy of the secondary photoelectrons, i. e. from the minimum value of the free electron parabola of onset energies of secondary electron emission as a function of emission angle that is determined by a parabolic fit [14].

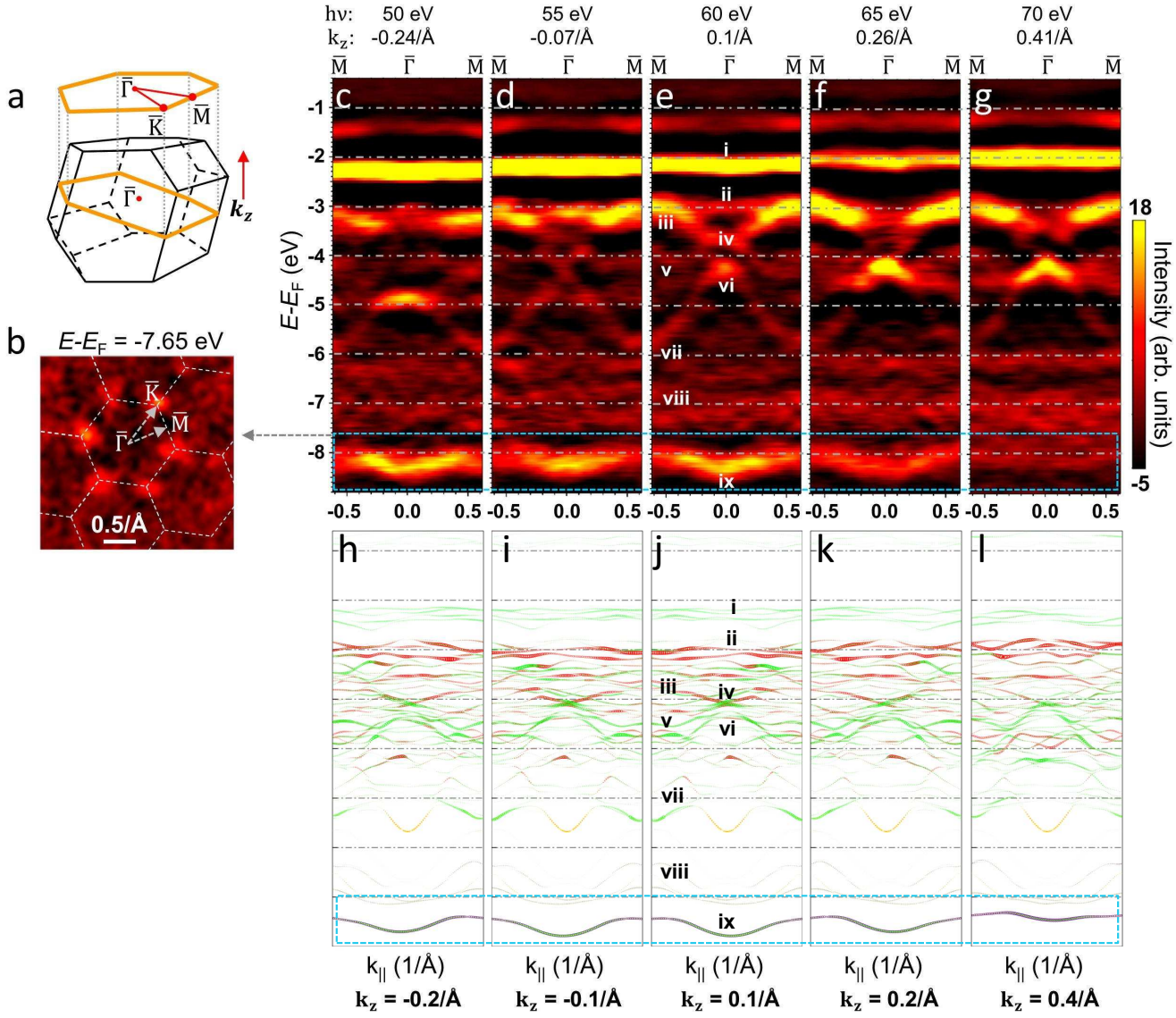

Figure S5. **Photon energy (k_z) variation.** (a) Sketch of the atomic bulk BZ of $NiPS_3$ (black) with 2D surface projection on top (orange) as well as corresponding cross section (orange). High symmetry points and $k_{||}$ directions (red lines) are marked. The upper/lower bulk BZ boundary is at $k_z = \pm 0.48/\text{Å}$. (b) (k_x, k_y) plot of ARPES curvature, E-E_F = -7.65 eV, $h\nu = 60\,\text{eV}$, $T = 45\,\text{K}$, hexagonal surface projections of the atomic BZ boundaries are overlaid (dashed white lines) (same as Fig. S1b). (c)-(g) ARPES curvature at various $h\nu$ as marked on top, $\overline{\text{M}\Gamma\text{M}}$ direction, $T = 45\,\text{K}$, k_z values maked on top are deduced using the free electron final state model (eq. (1)) with inner potential $V_0 = 12.1\,\text{eV}$ at $E - E_\text{F} \approx -3.7\,\text{eV}$. The k_z variation in each plot is $\Delta k_z \approx 0.25/\text{Å}$ with the largest value at the top. (h)-(l) Band structures from DFT+U at the k_z marked below, close to the k_z value of the ARPES data on top, $U_\text{eff} = 1.6\,\text{eV}$, only s, p_z, d_{z^2} orbitals, colorcode as in Fig. 3, main text. The blue, dashed rectangles mark a similar k_z dispersion of feature ix (P/S band). (c)-(l) share the same energy scale as displayed in c.

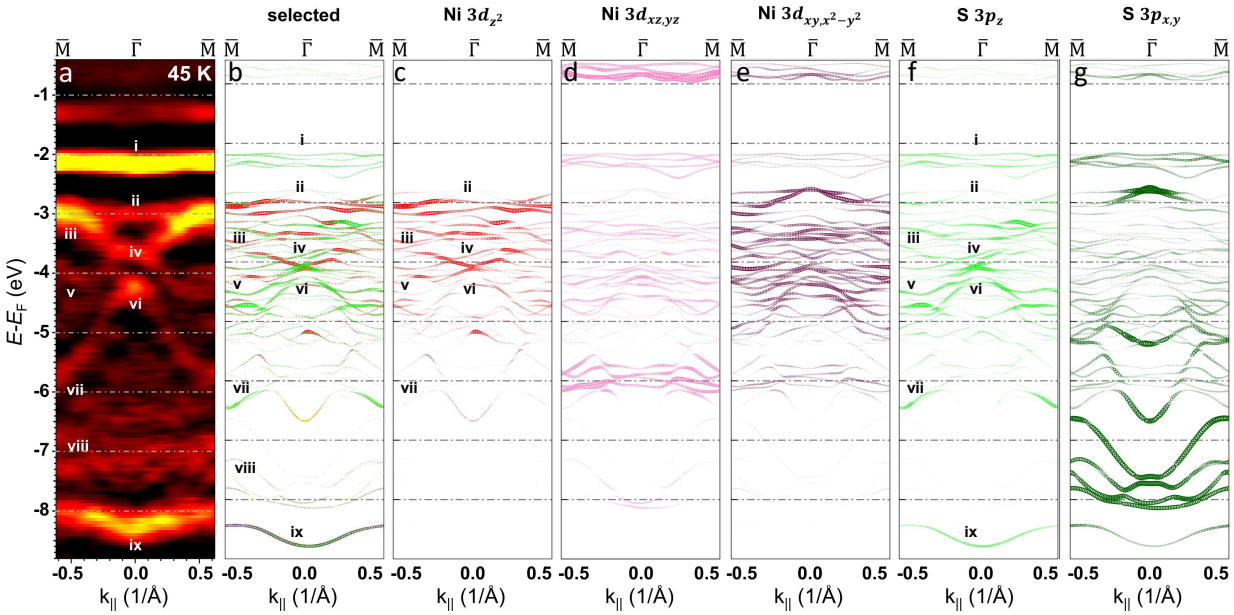

Figure S6. **Orbital projections of bands.** (a) ARPES curvature, $h\nu = 60\,\mathrm{eV}$, $T = 45\,\mathrm{K}$, $\overline{\mathrm{M\Gamma M}}$ direction, color scale as in Fig. 3, main text. (b)-(g) DFT+U band structure with selected orbitals as marked on top, $U_{\mathrm{eff}} = 1.6\,\mathrm{eV}$, $k_z = 0.1/\mathrm{Å}$, symbol diameter is proportional to the percentage of the orbital contribution to this state, color code as in Fig. 3, main text. Labels i-ix mark features discussed in the text.

To estimate V_0, we use the photoelectron intensity of the most relevant feature iv for $h\nu = 60\,\mathrm{eV}$ and emission angle $\theta = 0°$. It appears at $E^{\mathrm{A}}_{\mathrm{kin}} = 51.7\,\mathrm{eV}$ and is related to $k_{\parallel} = 0.0/\mathrm{Å}$ and $k_z = 0.1/\mathrm{Å}$ in the crystal as deduced from the comparison with the DFT+U data (Fig. S3, S4). Adequate rearrangement of eq. (1) and eq. (2) eventually results in [17]:

$$V_0 = \frac{\hbar^2}{2m}(nG_{\perp} + k_z)^2 - E^{\mathrm{A}}_{\mathrm{kin}} + \phi - \phi^{\mathrm{A}}, \qquad (3)$$

where $G_{\perp} = 0.9917/\mathrm{Å}$ is the reciprocal lattice vector of $NiPS_3$ normal to the surface [18] and n is an integer. The free choice of n gives an uncertainty in deducing V_0. At $n = 4$, eq. (3) results in the lowest positive value of $V_0 \approx 12.1\,\mathrm{eV}$, while, for $n = 5$, one obtains an unrealistically large $V_0 \approx 46.6\,\mathrm{eV}$ [19]. Thus, $n = 4$ is the most reasonable. Inserting it into eq. (3) and solving for k_z reveals the values for other photon energies at $\theta = 0°$ and $E - E_{\mathrm{F}} = -3.7\,\mathrm{eV}$ [17] as marked in Fig. S5c-g. The k_z value obviously varies with $E - E_{\mathrm{F}}$, respectively $E^{\mathrm{A}}_{\mathrm{kin}}$ for constant $h\nu$. Within the displayed $E - E_{\mathrm{F}}$ range of Fig. S5c-g, k_z changes by roughly $0.25/\mathrm{Å}$ (25 % of the BZ) with the largest k_z at the top of the images.

As a rough crosscheck of the k_z selection, we display the k_z dependence of the DFT+U data directly below the $h\nu$ dependent ARPES data. The k_z values are not perfectly adapted due to the finite $\boldsymbol{k}$ point density in the calculation, but since k_z varies with $E - E_{\mathrm{F}}$ at constant $h\nu$ anyhow, this does not matter. Favorably, several trends with k_z are found similarly in calculation and experiment. Firstly, feature ix (blue dashed rectangle) moves upwards and gets less dispersive for $k_z \geq 0.2/\mathrm{Å}$, both in ARPES and DFT+U data. Secondly, feature ii, corresponding to Ni $3d_{z^2}$ bands, moves upwards and gets more intense in dispersion from left to right, both for experiment and calculation. For negative k_z, the dispersion of the Ni $3d_{z^2}$ band ii is even largely identical between experiment and calculation. Thirdly, at negative k_z, there is a flat Ni 3d band below feature vi (Fig. S5h,i) that appears surprisingly similar in the experimental data (Fig. S5c,d). Note that the in-plane AFM structure of $NiPS_3$ breaks time-reversal symmetry for the k_z direction and, hence, enables different $E(k_{\parallel})$ at positive and negative k_z for the same $|k_z|$, as found in ARPES and DFT+U.

There are also some discrepancies such as the upward movement of feature i with increasing k_z in the ARPES

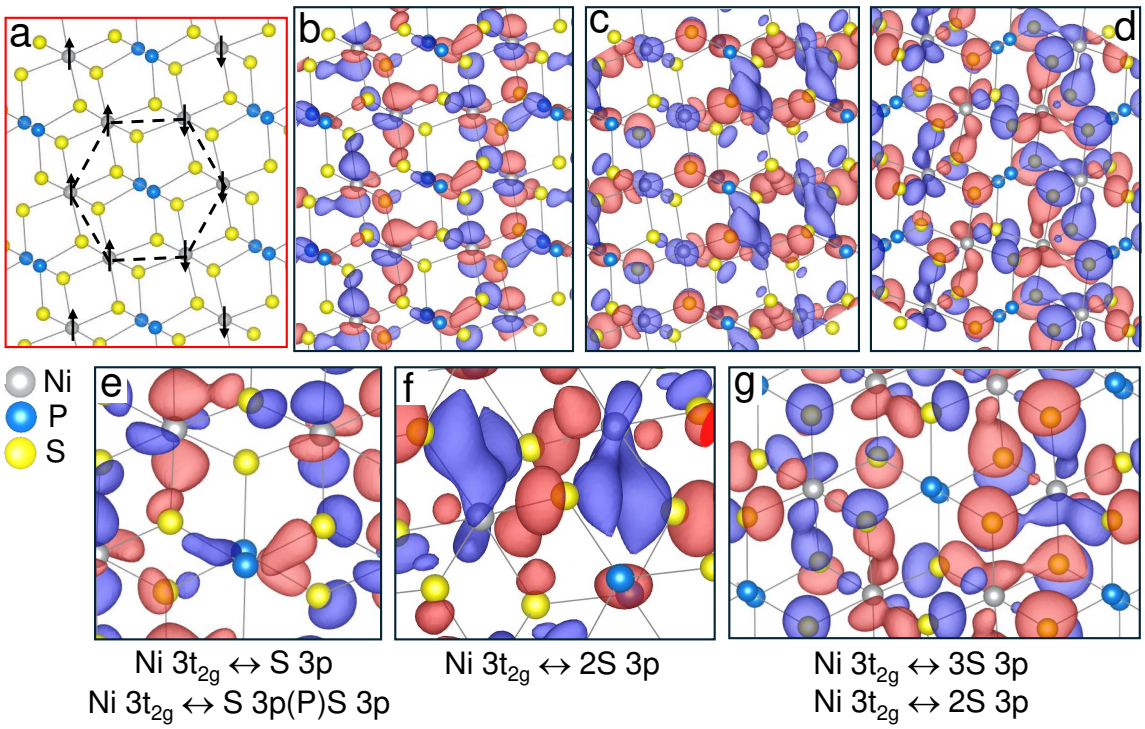

Figure S7. **Charge density of states from the magnetically modified energy range.** (a) Crystal structure of a single $NiPS_3$ layer viewed along the c axis with a marked honeycomb of six Ni atoms (dashed line) and spin directions in the zigzag AFM configuration (black arrows), same as Fig. 4a, main text. (b)–(d) Contour planes of the charge density $|\psi(\boldsymbol{x})|^2$ of three distinct states at $E - E_\mathrm{F} \approx -3.9\,\mathrm{eV}$ and $\boldsymbol{k} = \boldsymbol{0}/\text{Å}$ (marked by an arrow in Fig. 3c, main text). The area and angle of view are the same as in a. Blue and red contour planes mark opposite signs of the wave function. (e)–(g) Zoom into b–d, respectively, at an optimized angle of view showing the Ni bonds and orbitals more clearly. The identified bonds are indicated below (graphics made by VESTA [20]).

data, but not in the DFT+U data for an unknown reason.

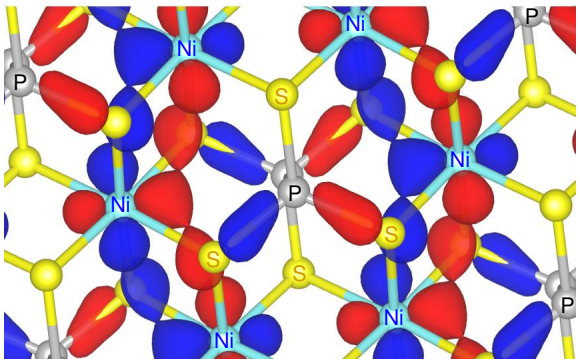

Figure S8. **Charge density of shifting band in Néel configuration.** Contour planes of the charge density $|\psi(\boldsymbol{x})|^2$ of a state at $E - E_\mathrm{F} = -3.9\,\mathrm{eV}$ and $\boldsymbol{k} = \boldsymbol{0}/\text{Å}$ in the Néel configuration with labeled atoms (zoom view, graphics made by VESTA [20]).

Nevertheless, $k_z = 0.1/\text{Å}$ appears to be a favorable choice for $h\nu = 60\,\mathrm{eV}$ at $E - E_\mathrm{F} = -3.7\,\mathrm{eV}$, i. e. the band energy region with changes across T_N.

Obviously, there is considerable k_z dispersion of the electronic band structure, both in the ARPES and the DFT+U data, revealing a sizable electronic interaction between the layers. Changes with $h\nu$ in the ARPES data might be partly due to changing matrix elements, but this is not the case for the k_z dependence of the DFT+U band structure.

S5. ORBITAL PROJECTIONS OF BANDS

Figure S6 shows the orbital contributions to the bands for all the Ni 3d and S 3p levels separately. Other orbitals have negligible contributions in that energy range except for the lowest energy band (feature ix) that is dominated by contributions of P $3p_z$ orbitals (Fig. 5a, main

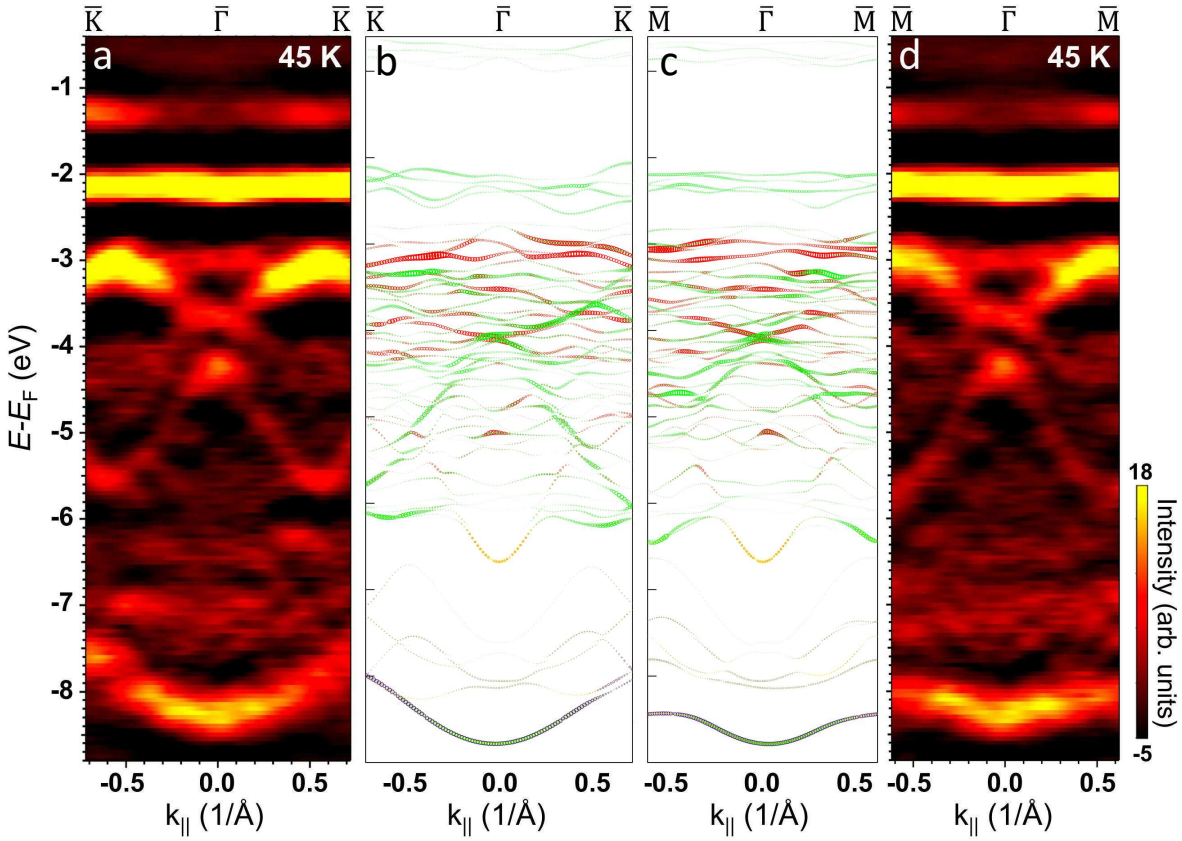

Figure S9. **Band structure in $\overline{\mathrm{K\Gamma K}}$ and $\overline{\mathrm{M\Gamma M}}$ direction.** (a), (d) ARPES curvature along $\overline{\mathrm{K\Gamma K}}$ and $\overline{\mathrm{M\Gamma M}}$ directions as marked on top, $h\nu = 60\,\mathrm{eV}$, $T = 45\,\mathrm{K}$. (b), (c) DFT+U band structure of only the s, p_z and d_{z^2} contributions, $U_{\mathrm{eff}} = 1.6\,\mathrm{eV}$, $k_z = 0.1/\mathrm{Å}$, symbol diameter is proportional to the percentage of the orbital contribution, color code as in Fig. 3, main text.

text). All the bands down to $E - E_{\mathrm{F}} = -5.5\,\mathrm{eV}$ have a mixed character of Ni 3d and S 3p orbitals, while the displayed bands at lower energy do not have any contributions from Ni orbitals. The topmost bands (feature i) have mostly S 3p character, but significant contributions from Ni $3\mathrm{d}_{xz,yz}$. The features ii-vi are dominated by Ni $3\mathrm{d}_{z^2}$ and Ni $3\mathrm{d}_{xy,x^2-y^2}$ character, however, with varying contributions from the different S 3 p orbitals. The changing band across T_{N} features Ni $3\mathrm{d}_{z^2}$ and $3\mathrm{d}_{xy,x^2-y^2}$ as well as S $3\mathrm{p}_z$ contributions of similar strengths. A bunch of bands at $E - E_{\mathrm{F}} \leq -5\,\mathrm{eV}$ consists of Ni $3\mathrm{d}_{xz,yz}$, $3\mathrm{d}_{xy,x^2-y^2}$ and S $3\mathrm{p}_{x,y}$ orbitals and, hence, is barely visible in the ARPES data via the simplified selection rules [11]. These bands are faintly apparent at $h\nu = 50 - 55\,\mathrm{eV}$ and $E - E_{\mathrm{F}} \approx -5\,\mathrm{eV}$ (Fig. S5c–d) due to a mixing with Ni $3\mathrm{d}_{z^2}$ (Fig. S5h–i). The bands between -6 eV and -8 eV have a nearly pure S $3\mathrm{p}_{x,y}$ character with minor contributions from P $3\mathrm{p}_{x,y}$ (not shown). In line, they appear only very faintly in the ARPES data at all $h\nu$. For feature ix, most contributions originate from P $3\mathrm{p}_z$ orbitals with smaller contributions from the various S 3p orbitals.

Most importantly, the energy range where bands change across T_{N}, i.e. feature iv (and maybe vi), exhibits a strong mixing of all Ni 3d and S 3p levels implying a multi-orbital hybridization. This directly reflects the S-mediated superexchange between nearest neighbor Ni atoms as discussed in the main text (Fig. 4, main text).

S6. ADDITIONAL CHARGE DENSITY PLOTS FOR STATES IN THE ENERGY RANGE CHANGING WITH TEMPERATURE

The identified energy range of the bands that shift with temperature (feature iv in Fig. S6a) contains four states at Γ as marked by the arrow in Fig. 3c, main text. The state

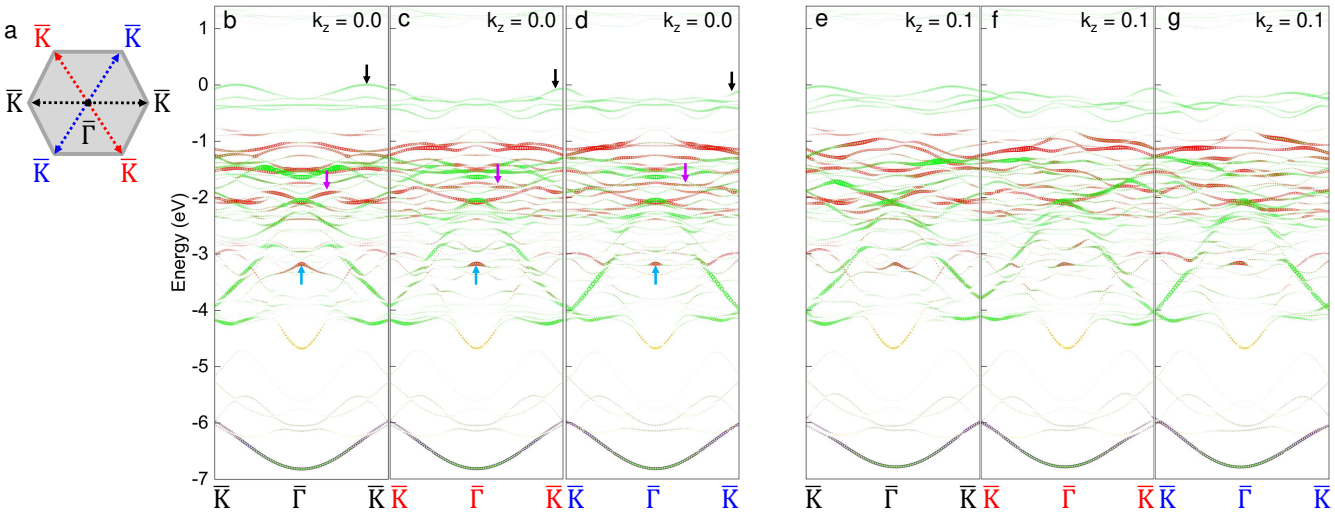

Figure S10. **Comparison of DFT+U band structure along non-equivalent $\overline{\mathrm{K\Gamma K}}$ directions.** (a) Scheme of the hexagonal 2D Brillouin zone with color coded $\overline{\mathrm{K\Gamma K}}$ directions. (b)-(d) DFT+U band structure along the three directions highlighted in a as marked by the $\boldsymbol{k}_{\parallel}$-axis symbol colors, only s, p_z and d_{z^2} contributions, $U_{\mathrm{eff}} = 1.6\,\mathrm{eV}$, $k_z = 0.0/\text{Å}$, symbol diameter is proportional to the percentage of the orbital contribution, color code as in Fig. 3, main text. Minor differences are highlighted by arrows. (e)-(g) Same as b-d, but for $k_z = 0.1/\text{Å}$. The asymmetry between the positive and the negative $\overline{\Gamma\mathrm{K}}$ directions are due to the missing mirror symmetry in the Brillouin zone planes perpendicular to k_z (Fig. S5a).

that exhibits a charge density compatible with a nearest neighbor Ni $3t_{2g}$-S 3p-Ni $3t_{2g}$ superexchange path is plotted in Fig. 4, main text. The other three states are shown in Fig. S7. None of them couples Ni atoms. Again the charge density is distinct in the ferromagnetically coupled zigzag chains of opposite spin direction. For the state in Fig. S7b and e, the left zigzag chain (↑), corresponding to the upper left Ni atom in Fig. S7e, shows a Ni $3t_{2g}$ orbital. This orbital is coupled to one S 3p level via its top lobe. The bottom lobe also couples to a S 3p-orbtal that itself is tilted towards a P-atom that is also connected to two S 3p lobes on the other side. In the other zigzag chain (↓, upper right Ni atom in Fig. S7e), the Ni atom exhibits a nearly unperturbed $3t_{2g}$ orbital.

The state in Fig. S7c and f shows uncoupled S 3p and Ni $3t_{2g}$ orbitals in the left zigzag row (not visible in f). The two red in-plane lobes of the Ni $3t_{2g}$ orbital are asymmetrically perturbed, but do not overlap with any neighbors also at larger extension of the contour planes (not shown). In contrast, the Ni $3t_{2g}$ orbitals in the right zigzag row show one blue lobe each that couples relatively strongly to two neighboring S 3p orbitals. But again, this charge density is not connected to neighboring Ni atoms. A minor charge density is also found between the two P atoms of the dumbbell. For the last state at this energy (Fig. S7d and g), the Ni atoms in both rows show $3t_{2g}$ orbitals interacting with neighboring S 3p orbitals. In the left zigzag row, the upper and the lower lobes exhibit overlap with an adjacent S 3p orbital. This is most clearly visible in Fig. S7g for the Ni atoms with interacting red lobes at top and bottom, where both coupled S atoms are in front of the Ni atom. For the right zigzag row, one lobe of the Ni $3t_{2g}$ orbital interacts with one and the other with two neighboring S 3p orbitals. But again, all these bonds are dead ends for connecting to neighboring Ni atoms. Hence, none of the three states exhibits any exchange path, such that it is indeed likely that the state displayed in Fig. 4, main text, is the one that changes its energy across T_{N}.

Interestingly, the same energy region for the Néel configuration (Fig. 3e, main text) shows a state that features a third nearest-neighbor exchange path (Fig. S8). The most left Ni $3t_{2g}$ orbital has a touching point for its right, red lobe to two adjacent S 3p orbitals (red lobes as well). The same applies to the most right Ni $3t_{2g}$ orbital concerning its left, blue lobe interacting with the blue lobes of two adjacent S 3p orbitals. These touching points of lobes evolve into a merging charge density for more extended contour planes (not shown) corroborating its bonding nature. Intriguingly, the opposite lobes of the four involved S 3p orbitals are extended towards the intermediate P dumbbell such that they can interact pairwise at the position of one P atom as again corroborated by a charge density merger at more extended contour planes (not shown). Hence, each of the central P atoms medi-

ates a third nearest neighbor exchange of Ni atoms via Ni $3t_{2g}$-S 3p-S3p-Ni $3t_{2g}$ without involving its own orbitals. A similar configuration has recently been proposed to be responsible for the strong third nearest neighbor exchange interaction in $NiPS_3$ amounting to $J_3 = -6.5\,\mathrm{meV}$ [21, 22], however, involving two Ni $3e_g$ orbitals [23].

We checked also the charge distribution of other states in a broader energy range for both, the zigzag and the Néel configuration, but without achieving any further reportable insight.

S7. ELECTRONIC BAND STRUCTURE IN $\overline{\mathrm{K\Gamma K}}$ DIRECTION

Figure S9 shows the comparison of the band structures in $\overline{\mathrm{K\Gamma K}}$ and $\overline{\mathrm{M\Gamma M}}$ direction, both for ARPES at $h\nu = 60\,\mathrm{eV}$ and corresponding DFT+U data ($U_{\mathrm{eff}} = 1.6\,\mathrm{eV}$, $k_z = 0.1/\text{Å}$). The band structure in the two directions is rather similar in ARPES and DFT+U, with minor changes of $k_\parallel$ dispersion. Some similarities appear in the dispersion change between ARPES and DFT+U. For example, the low energy P 3p/S 3p band at $E - E_{\mathrm{F}} \approx -8.5\,\mathrm{eV}$ is more parabolic up to the BZ boundary in $\overline{\Gamma\mathrm{K}}$ direction for ARPES and DFT+U. Moreover, comparing the dispersion around $\overline{\mathrm{K}}$ and $\overline{\mathrm{M}}$, the upwards dispersion towards $\overline{\mathrm{M}}$ at $E - E_{\mathrm{F}} \approx -4\,\mathrm{eV}$ is also visible in DFT+U, but in both cases not around $\overline{\mathrm{K}}$. Similarly, the upwards dispersion towards $\overline{\mathrm{K}}$ at $E - E_{\mathrm{F}} \approx -5.5\,\mathrm{eV}$, not apparent towards $\overline{\mathrm{M}}$ in ARPES, coincides with a more flat steepness along $\overline{\Gamma\mathrm{K}}$ in DFT+U.

S8. COMPARISON OF DFT+U BAND STRUCTURE ALONG NON-EQUIVALENT $\overline{\mathrm{K\Gamma K}}$ DIRECTIONS

Figure S10 compares the DFT+U band structures along the three $\overline{\mathrm{K\Gamma K}}$ directions in the hexagonal BZ. These directions are non-equivalent in the magnetic zigzag configuration via the resulting rectangular BZ (Fig. S1a). Indeed the band structures exhibit minor differences as highlighted by arrows in Fig. S10b-d, but they are well below 100 meV or burried into bunches of bands. Hence, they are rather challenging to be observed in our experiment with energy resolution of 50 meV and typical peak widths above 200 meV (Fig. 2c,f, main text, Suppl. Fig. S12b-c). Moreover, since the 3D BZ is not mirror symmetric perpendicular to k_z except at $k_z = 0/\text{Å}$ (Fig. S5a), the projected directions as probed by ARPES are already non-equivalent without magnetic symmetry breaking. Most strikingly, the positive and negative $\overline{\Gamma\mathrm{K}}$ directions become non-equivalent by the 3D BZ shape leading to distinct not point-symmetric dispersions (Fig. S10e-g) as partially also apparent in the experimental data (Fig. S5b-g). Both complicates the detection of magnetically induced symmetry breakings additionally.

S9. COMPARING ZIGZAG AND DISORDERED MAGNETIC CONFIGURATIONS

Figure S11 compares the band structure of $NiPS_3$ for the zigzag AFM ground state and a randomly disordered configuration of atomic spins in a $4 \times 2 \times 3$ supercell with zero net magnetic momentum in the supercell (Fig. S11a). The latter is a reasonable approximation of the paramagnetic case [14, 24]. In both cases, we unfold to the atomic, hexagonal surface BZ (Fig. S5a). Here, we only display the intensity of the bands after unfolding (Fig. S11b, c), since a projection to individual orbitals is rather challenging after unfolding the extremely small BZ of the disordered configuration. For assignment, we add the element specific partial density of states (pDOS) of the zigzag AFM configuration (left to the band structures).

Comparing the band structures (Fig. S11b–c), one observes large similarities including a barely changed fundamental band gap at $E = 0-1\,\mathrm{eV}$. In the energy range with significant Ni 3d contribution of both spin directions, the bands are more blurred in the paramagnetic phase. This is likely due to the different energies of various Ni atoms due to their different local spin environment. Notice that the contribution of each Ni atom is projected to the same $k_\parallel$ via the unfolding, since the Ni atoms with different spin are forced into the corresponding periodicity of the smaller unit cell. Consistently, bands with pure S or P character are barely blurred since they are largely periodic in the smaller unit cell.

Importantly, the most striking band change appears at the crossing point (at $\overline{\Gamma}$, $E \approx -2\,\mathrm{eV}$, white arrows in Fig. S11b) that we identified as the region of band shift in the ARPES experiment. The lower part of the crossing moves upwards by about 150 meV (dashed line) and broadens in the paramagnetic phase. This corroborates that this energy region is indeed very sensitive to the magnetic configuration, albeit the changes could not be reproduced quantitatively via this simplified version of a paramagnetic state.

Nevertheless, the favorable comparison demonstrates that modeling the paramagnetic phase by spin disorder reveals important insights, in that case corroborating the assignment of changing bands in the experiment. This is good news regarding the extensive computational cost of finite temperature calculations, in particular for large unit

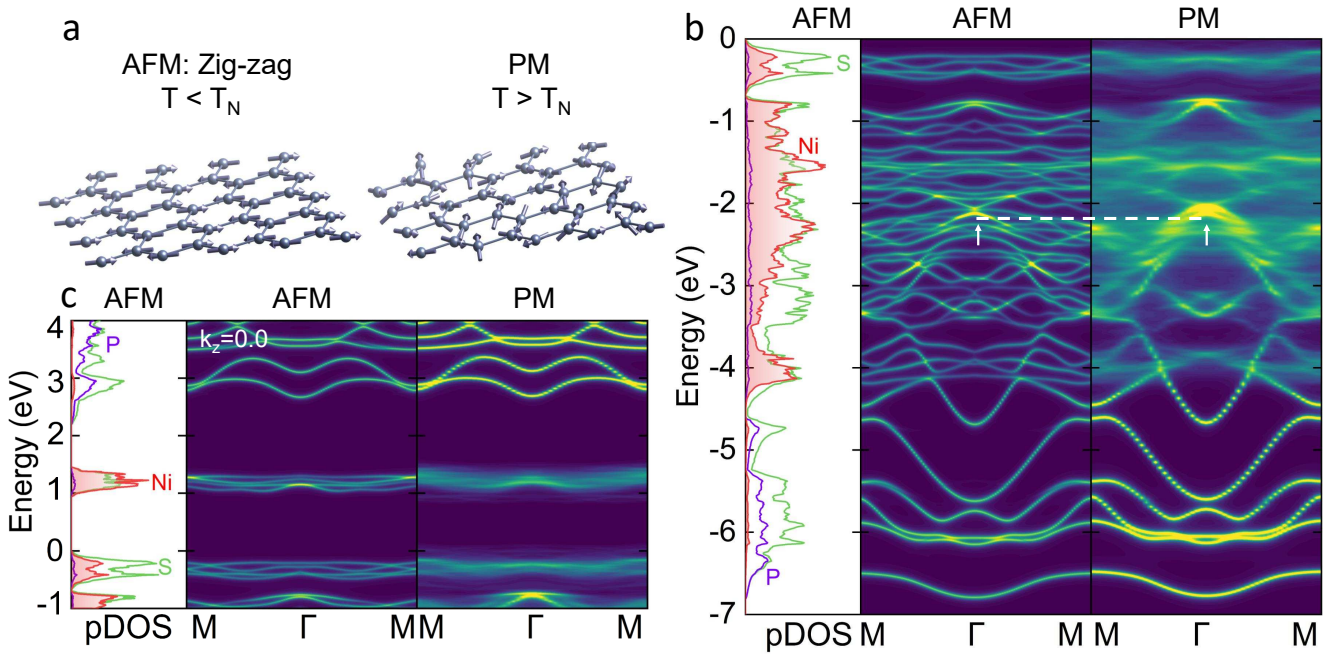

Figure S11. **Antiferromagnetic vs. paramagnetic band structure.** (a) Spin arrangement of the atoms for the calculated antiferromagnetic (AFM) zigzag and the spin-disordered, paramagnetic (PM) state. (b) Projected density of states (pDOS) of the AFM zigzag configuration for the three different elements (left) and electronic band structure for both, the AFM zigzag and the PM state (right). Only states below the valence band maximum (0 eV) are displayed. Dashed, horizontal line stresses the upwards shift of the bands marked by an arrow by roughly 150 meV. (c) Same as b, but for states with $E > -1$ eV.

cells and significant correlations as in the case of $NiPS_3$ [24].

S10. ARPES FEATURE NOT COVERED BY DFT+U CALCULATION

Figure S12 shows the additional feature observed at $E - E_F \approx -1.3$ eV in more detail. The raw $I(E, k_\parallel)$ plot reveals a sizable contrast change at the corresponding energy (Fig. S12a, arrow) implying that it is a real structure. Energy distribution curves at Γ show the feature as a shoulder below the peak of the valence band maximum at $E - E_F \approx -2.2$ eV (Fig. S12b). The energy position and height of the shoulder are nearly identical above and below T_N. However, the shoulder shifts upwards in energy with increasing $h\nu$ very similarly to the valence band maximum (Fig. S12c). This parallel upwards shift can be seen more clearly in the curvature plots of Fig. S5c-g, where both barely dispersive features move upwards by roughly 200 meV in parallel between $h\nu = 50$ eV and $h\nu = 70$ eV. Hence, the shoulder is robust and appears to be tied to the valence band maximum. As mentioned in the main text, its origin will be discussed in a separate publication.

S11. COMPARISON OF THE FULL ENERGY RANGE OF THE ARPES DATA ABOVE AND BELOW T_N.

Fig. S13 shows the full energy range of the ARPES data recorded above and below T_N in comparison with the optimized DFT+U data of the band structure. For the latter, we again display only the bands that are recorded according to the simplified selection rules [11]. One recognizes that changes only appear in the energy range of $E - E_F = -3$ to -4 eV. In particular, the assignement of the calculated band structure via U_{eff} (Fig. S3) and k_z (Fig. S4) is not influenced by these minor changes. Hence, the calculated band structure fits nicely to the ARPES data above and below T_N except of the mysterious structure at $E - E_F = -1.3$ eV.

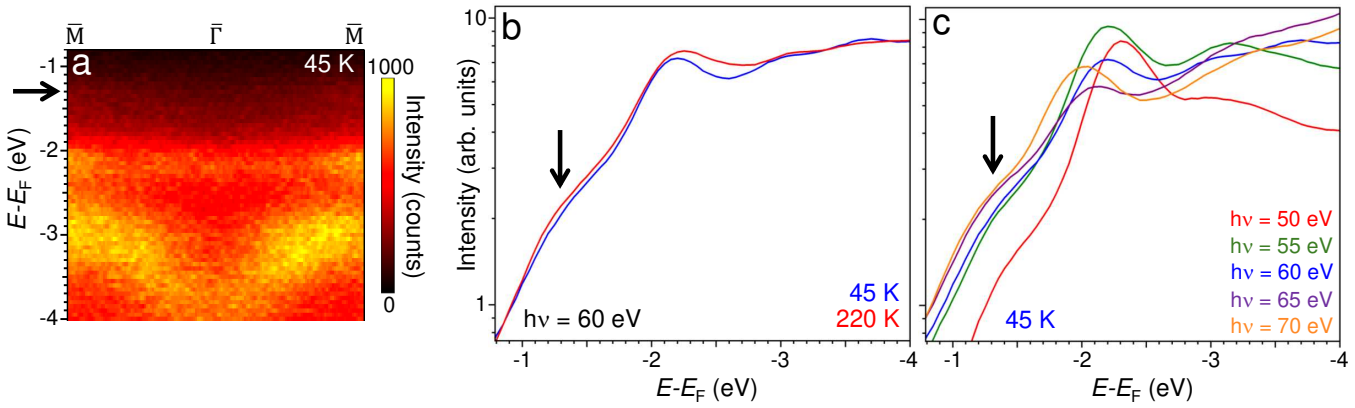

Figure S12. **Spectral shoulder not explained by DFT+U.** (a) Raw ARPES data, $h\nu = 60\,\mathrm{eV}$, $T = 45\,\mathrm{K}$ (Zoom into Fig. 2b, main text). (b) Smoothed energy distribution curves at $\bar{\Gamma}$ (box smoothing of two energy pixels (100 meV)), T as marked, $h\nu = 60\,\mathrm{eV}$. (c) Same as b at various $h\nu$, $T = 45\,\mathrm{K}$. The arrow in a-c is consistently at $E - E_\mathrm{F} = -1.3\,\mathrm{eV}$, i. e. at the ARPES feature for $h\nu = 60\,\mathrm{eV}$ not covered by DFT+U calculations (Fig. 3c-d, main text).

S12. ARPES CURVATURE

In the main text as well as in the supplementary information, we partially use ARPES curvature plots. This enables for better visibility of the bands [25]. The curvature $C(E)$ is calculated with respect to energy E after smoothing the raw data, as described in the caption of Fig. 2c, main text, via:

$$C(E) = \frac{-I''(E)}{(C_0 + I'(E)^2)^{3/2}} \quad \text{with} \quad C_0 = a_0 |I'(E)|^2_{\max}. \tag{4}$$

Here, I' and I'' are the first and second partial derivative with respect to energy of the smoothed photoelectron intensity $I = I(E, k_\parallel)$, $|I'(E)|_{\max}$ is the maximum value of the first partial derivative, while a_0 is a free parameter used to adjust the relative intensity of different bands for better visibility. We have consistently used $a_0 = 0.05$.

To highlight the advantage of using curvature instead of the second derivative, we shortly describe its origin. The curvature $C(x)$ of a function $y := f(x)$ measures the change of angle φ of a graph's tangent with respect to the path length s along the graph. This reads

$$C(x) = -\frac{d\varphi}{ds} = -\frac{d\varphi}{dx}\frac{dx}{ds} = -\frac{f''(x)}{\left(1 + (f'(x))^2\right)^{\frac{3}{2}}} \tag{5}$$

with $\tan\varphi(x) = \frac{dy}{dx} = f'(x)$ [26]. The negative sign is chosen to identify relative maxima of $f(x)$ with the maxima of $C(x)$. $C(x)$ features the local inverse radius $1/R$ of the $y(x)$ plot, but only if x and y are equally scaled and, hence, have the same unit. For example, a full circle then implies directly $d\varphi/ds = 2\pi/(2\pi R) = 1/R$. Typically, the smallest tangential circles are found at the local maxima of a curve (Fig. S14a). Consistently, a local maximum in $f(x)$ implies that $f'(x)$ vanishes while $-f''(x)$ has a large, positive value, such that the corresponding $C(x)$ mostly exhibits a local maximum, too. Importantly, the curvature showcases the inverted parabola area around a peak more directly than the second derivative. If one considers a purely inverted parabola $y = -x^2 + 4$, it exhibits a peak in curvature at its maximum $\left(C(x) = \frac{2}{(1+4x^2)^{3/2}}\right)$, while the 2$^{\mathrm{nd}}$ derivative remains constant (Fig. S14b).

These favorable properties of the curvature persist, if y and x have different units as in the $I(E)$ curves of the ARPES data. However, a local radius of a curve is then not well defined due to the unit mismatch. Hence, the 1 in the sum of the denominator of eq. (5) gets arbitrary, besides having the wrong unit [25]. Consequently, C_0 is introduced in eq. (4) that can be used as a tuning parameter balancing between the first and the second derivative as the two benchmarks of a local peak position.

Reducing C_0 strengthens real maxima by the divergence of $1/f'(x)^3$ (Fig. S14b). In contrast, increasing C_0 strengthens the $-f''(x)$ term and, hence, highlights shoulders in the ARPES data that originate from peaks on top of a background intensity. The optimal value of C_0 has to be chosen visually by careful comparison to the raw $I(E)$ data such that reproducible shoulders as in Fig.

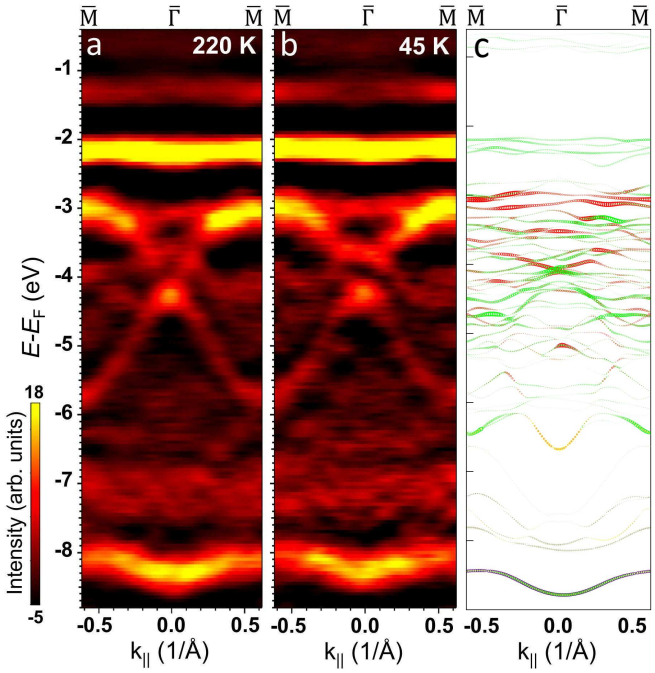

Figure S13. **ARPES data above and below T_N compared to DFT+U data.** (a) ARPES curvature along $\overline{\mathrm{M\Gamma M}}$ direction, $h\nu = 60\,\mathrm{eV}$, $T = 220\,\mathrm{K}$. (b) ARPES curvature along $\overline{\mathrm{M\Gamma M}}$ direction, $h\nu = 60\,\mathrm{eV}$, $T = 45\,\mathrm{K}$. (c) Calculated band structure by DFT+U, $U_{\mathrm{eff}} = 1.6\,\mathrm{eV}$, $k_z = 0.1/\mathrm{Å}$, only bands with significant s, p_z and d_{z^2} character are displayed [11], same as Fig. S3d.

S12b-c appear as features in $C(E)$ while apparent noise does not.

S13. COMPARISON BETWEEN DFT+U, HYBRID FUNCTIONALS AND GW CALCULATIONS

In this section, we clarify our rationale for using the DFT+U framework. We support our choice with additional calculations using hybrid functionals and post-DFT methods such as GW.

The effective Hubbard parameter U_{eff} is not a universal constant, but rather depends strongly on the specific modeling framework. Its numerical value is sensitive to the choice of exchange–correlation functional, the inclusion of van der Waals corrections, and the type of projector or localized basis used for defining the correlated orbitals. As a consequence, reported values of U_{eff} in the literature span a wide range, even for nominally similar materials. For example, in the literature on NiO, values between 4 eV and 8 eV are commonly employed [27–30], whereas for layered chalcogenides such as $TlNi_2Se_2$, smaller values (2–3 eV) can be found [31]. Importantly, our selection of $U_{\mathrm{eff}} = 1.6\,\mathrm{eV}$ is not arbitrary, but is guided by its ability to largely reproduce the details of the valence-band structure as observed in ARPES, which is central to the interpretation of the electronic structure presented in this manuscript.

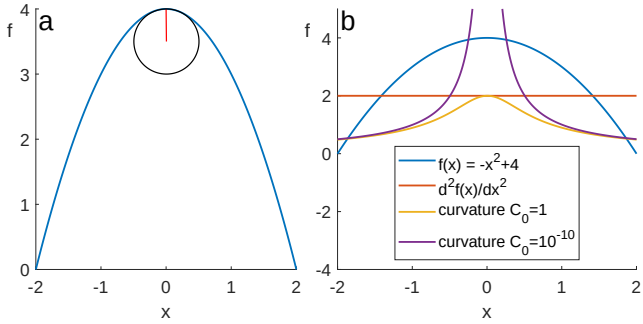

Figure S14. **Curvature versus second derivative** (a) Exemplary function $f(x) = -x^2 + 4$ with tangential circle at $f(x = 0)$. The radius $R = 0.5$ is marked in red. (b) The same $f(x)$ as in (a) (blue) is plotted together with the 2nd derivative $d^2f(x)/dx^2$ (orange) and curvature $C(x)$ according to eq. (4) with two different parameters C_0 (yellow, violet).

Additionally, it is well established that experimental estimates of effective Coulomb interactions are themselves method-dependent. Different spectroscopic techniques (e.g., XPS, EELS, ARPES) probe distinct excitations and screening environments and therefore often yield different effective interaction strengths. This variation does not indicate a shortcoming of DFT+U, but rather stems from the fundamental difference between the quantities accessible in experiment—typically related to excited states—and those described by DFT, which is a ground-state theory. In principle, there exists a single value of U_{eff} that would correctly complement the exchange–correlation functional to reproduce both ground-state and excitation properties. However, this value is generally not known *a priori*, and different attempts to extract it from experiment or theory can yield different results depending on how closely the measured excitation reflects the underlying ground-state properties. Importantly, no existing electronic-structure formalism—whether DFT+U, hybrid functionals, or GW—can completely eliminate this ambiguity, as each relies on different approximations and levels of treatment of electronic screening.

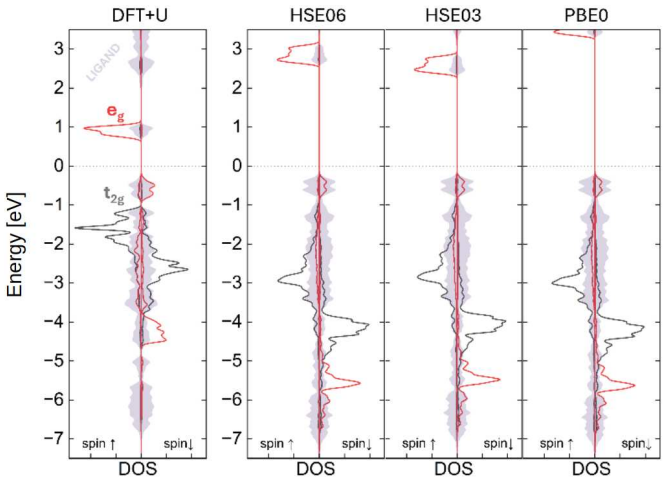

Figure S15. Comparison between the orbital-projected, spin-polarized density of states (DOS) calculated using DFT+U (U_{eff}=1.6 eV) and various exchange–correlation functionals as HSE06, HSE03, and PBE0, red: Ni $3e_g$-, black: Ni $3t_{2g}$-, grey: ligand orbitals. Both, HSE03 and HSE06 employ an exact-exchange fraction of 0.25. Notice that the gap in HSE03, HSE06 and PBE0 is significantly larger than experimentally observed: $E_{\mathrm{g}} = 1.8\,\mathrm{eV}$ [15].

To compare our calculations with alternative approaches to the exchange-correlation energies, we firstly present the comparison between the DFT+U with hybrid functionals such as HSE06 [32], HSE03 [33], or PBE0 [34] (Fig. S15). All hybrid functional calculations employ the optimized geometry within the PBE+U framework (with $U = 1.6\,\mathrm{eV}$) including D3 van der Waals corrections. It is well established that the critical parameter in such functionals is the fraction of the Hartree–Fock exchange. It has a direct and significant impact on the relative energies of the correlated 3d states (Fig. S16). The default fraction of 25% of Hartree-Fock exchange systematically overlocalizes the Ni 3d orbitals. This leads to a disagreement with ARPES measurements, in particular, the pronounced Ni $3e_g$ contribution at $E \in [-5\,\mathrm{eV}, -6\,\mathrm{eV}]$ is not found by ARPES. Reducing the fraction of the Hartree-Fock exchange restores the agreement with the DFT+U at $U_{\mathrm{eff}} = 1.6\,\mathrm{eV}$ (Fig. S16) and, hence, with the ARPES data, but this amounts to the same type of empirical adjustment that one performs with U_{eff} in DFT+U. In particular, with 10% of Hartree-Fock exchange, one reproduces the DFT+U results at the chosen $U_{\mathrm{eff}} = 1.6\,\mathrm{eV}$ (Fig. S16), while higher percentages reveal the same trends as larger U_{eff} in DFT+U (not shown, but compare to Fig. S3b-g). This illustrates the close analogy between tuning the fraction of Hartree–Fock exchange and adjusting the Hubbard U_{eff} parameter. Importantly, no additional band is appearing above the valence band maximum, while only the Ni 3d levels are shifted downwards in the valence band and upwards in the conduction band with increasing percentage of the exact exchange contribution (Fig. S16).

This highlights that hybrid functionals are not entirely parameter-free when applied to materials with correlated electrons. In practice, they often require empirical adjustments, e. g., to reproduce experimental band gaps or other key properties, conceptually analogous to the tuning of the U parameter in DFT+U. However, while U acts directly on localized d-states, hybrid functionals affect all electronic states through the inclusion of exact exchange. For this reason, we consciously decided not to employ hybrid functionals in this study. Although their use would, in principle, be technically feasible, their computational cost renders them impractical for the large-scale simulations required here (e.g., performing Brillouin zone unfolding).

We also carried out G0W0 [35] and partially self-consistent EVGW0 [36] calculations using the optimized structure calculated within PBE+U framework ($U = 1.6\,\mathrm{eV}$) including D3 van der Waals corrections (Fig. S17). For the GW calculations, we employed PAW pseudopotentials adapted for GW computations. In the GW implementation, we used a fully frequency-dependent approach without the plasmon-pole approximation. The number of bands was set to approximately ten times the number of occupied bands for both the G0W0 and EVGW0 approaches. For the EVGW0 method, four self-consistency (scfGW) iterations were performed to ensure convergence. These approaches provide a rigorous quasiparticle correction to the Kohn-Sham band structure, but their effect strongly depends on the starting point. Namely, in our case, they do not lead to significant changes in the ordering of the t_{2g} and e_g manifolds, but just to an increase of the fundamental band gap and a relatively small upwards shift of all bands (Fig. S17). Moreover, they do not exhibit an additional band feature above the valence band maximum such as our ARPES feature at $E - E_{\mathrm{F}} = -1.3\,\mathrm{eV}$. Instead, a slight narrowing of the prominent Ni 3d peaks is found (Fig. S17). These observations are consistent with the well-known sensitivity of GW to the underlying mean-field reference. We would like to stress that GW methods are extremely powerful in addressing excitation-related phenomena, such as band-gap renormalization or excitonic effects, and they have been widely applied to such problems. Their main advantage, however, lies in the treatment of quasiparticle excitations rather than in correcting the relative position of strongly localized 3d orbitals in transition-metal

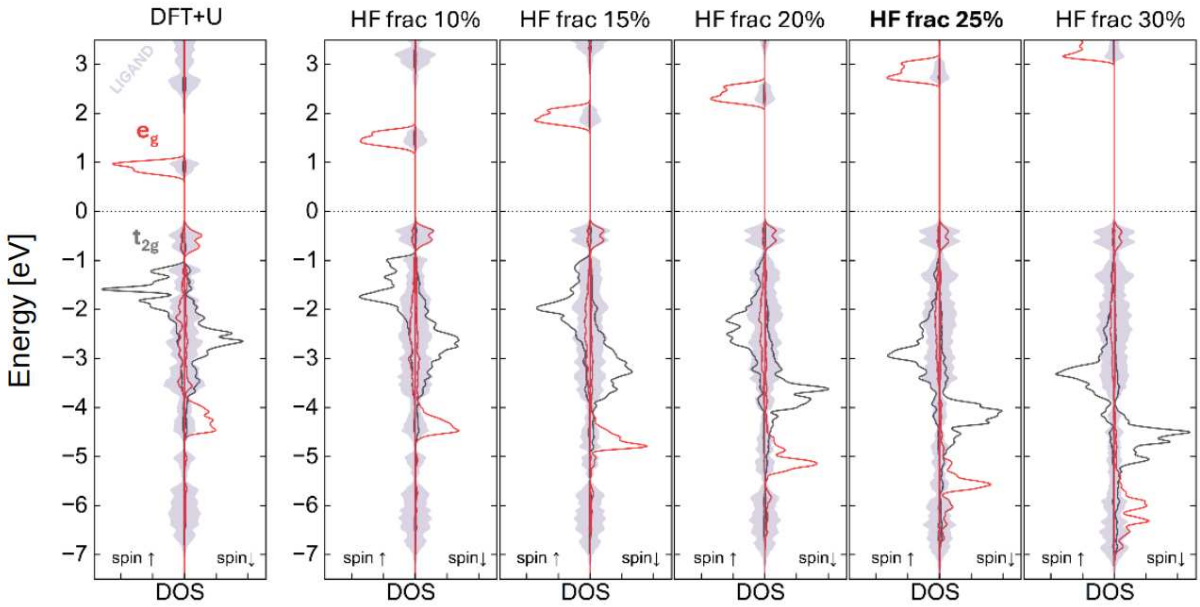

Figure S16. Comparison between the orbital-projected, spin-polarized DOS calculated using DFT+U ($U_{\text{eff}} = 1.6\,\text{eV}$) and hybrid functionals with different fractions of the exact exchange.

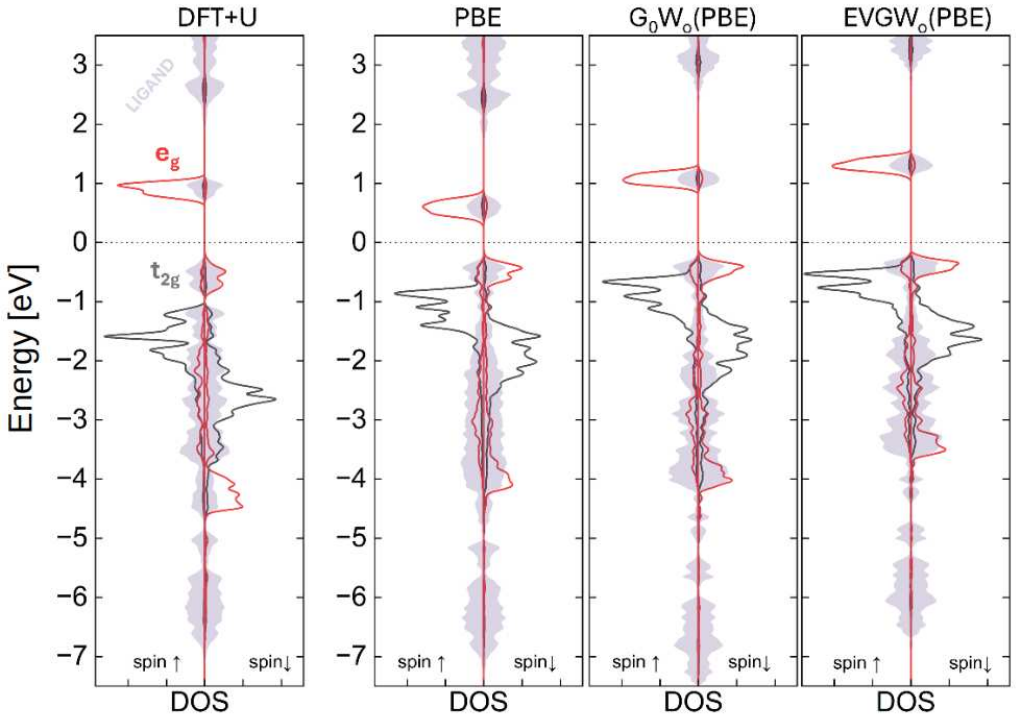

Figure S17. Comparison between the orbital-projected, spin-polarized DOS using DFT+U ($U_{\text{eff}} = 1.6\,\text{eV}$) as well as calculations with quasiparticle corrections to the Kohn-Sham density of states using G0W0 and partially self-consistent EVGW0 calculations on top of PBE.

chalkegonides. For the latter, DFT+U remains a simpler and more robust choice.

In summary, our extended benchmark calculations confirm that neither hybrid functionals nor GW approaches capture the additional ARPES feature at $E - E_F = -1.3\,\text{eV}$. The discrepancy is therefore not attributable to the choice of DFT+U. Importantly, DFT+U offers unique advantages that make it the most appropriate method for this study. Namely, it allows for a computationally tractable description of the paramagnetic state and the unfolding of electronic structures into a different supercell as required for comparison with the ARPES data. This would not be feasible with hybrid functionals or GW due to their computational cost. Furthermore, a comparison of $NiPS_3$ with related compounds such as $MnPS_3$ (Fig. 5, main text), where DFT+U was successful in capturing all bands found by ARPES, indicates that one generally should not expect additional bands in the electronic structure beyond those reproduced by DFT+U. Any further splitting of ligand-derived states or localized d-manifolds would in fact be surprising given the crystal symmetry of this class of materials. This strongly suggests that the additional feature observed in ARPES above the valence-band maximum cannot be rationalized within a mean-field framework, but rather reflects physics that goes beyond standard DFT-based methods.

REFERENCES

[1] Bae, Y. J. et al. Exciton-coupled coherent magnons in a 2D semiconductor. *Nature* **2022**, *609*, 282–286.

[2] Sahu, S.; Chauhan, A.; Ghosh, P.; Routh, S.; Puranik, R.; Thirupathaiah, S.; Lal, S.; S, S. P.; Mitra, C.; Kamaraju, N. Ultrafast Dynamics of Spin-Orbit Entangled Excitons Coupled to Magnetic Ordering in van der Waals Antiferromagnet NiPS3. 2025; `https://arxiv.org/abs/2509.04900`.

[3] Vogt, K.; Fradin, F.; Pearson, J.; Sebastian, T.; Bader, S.; Hillebrands, B.; Hoffmann, A.; Schultheiss, H. Realization of a spin-wave multiplexer. *Nature Communications* **2014**, *5*.

[4] Au, Y.; Ahmad, E.; Dmytriiev, O.; Dvornik, M.; Davison, T.; Kruglyak, V. V. Resonant microwave-to-spin-wave transducer. *Applied Physics Letters* **2012**, *100*.

[5] Zhang, X.; Zou, C.-L.; Jiang, L.; Tang, H. X. Strongly Coupled Magnons and Cavity Microwave Photons. *Physical Review Letters* **2014**, *113*.

[6] Diederich, G. M.; Cenker, J.; Ren, Y.; Fonseca, J.; Chica, D. G.; Bae, Y. J.; Zhu, X.; Roy, X.; Cao, T.; Xiao, D.; Xu, X. Tunable interaction between excitons and hybridized magnons in a layered semiconductor. *Nature Nanotechnology* **2022**, *18*, 23–28.

[7] Wang, X.; Cao, J.; Lu, Z.; Cohen, A.; Kitadai, H.; Li, T.; Tan, Q.; Wilson, M.; Lui, C. H.; Smirnov, D.; Sharifzadeh, S.; Ling, X. Spin-induced linear polarization of photoluminescence in antiferromagnetic van der Waals crystals. *Nat. Mater.* **2021**, *20*, 964–970.

[8] Belvin, C. A.; Baldini, E.; Ozel, I. O.; Mao, D.; Po, H. C.; Allington, C. J.; Son, S.; Kim, B. H.; Kim, J.; Hwang, I.; Kim, J. H.; Park, J.-G.; Senthil, T.; Gedik, N. Exciton-driven antiferromagnetic metal in a correlated van der Waals insulator. *Nat. Commun.* **2021**, *12*, 4837.

[9] Wang, H.; Du, C.; Hammel, P. C.; Yang, F. Antiferromagnonic Spin Transport from $Y_3Fe_5O_12$ into NiO. *Phys.Rev.Lett.* **2014**, *113*, 097202.

[10] Popescu, V.; Zunger, A. Extracting E versus k effective band structure from supercell calculations on alloys and impurities. *Phys. Rev. B* **2012**, *85*, 085201.

[11] Moser, S. An experimentalist's guide to the matrix element in angle resolved photoemission. *J. Electr. Spectr. Rel. Phen.* **2017**, *214*, 29–52.

[12] Ouvrard, G.; Brec, R.; Rouxel, J. Structural determination of some MPS3 layered phases (M = Mn, Fe, Co, Ni and Cd). *Mater. Res. Bull.* **1985**, *20*, 1181–1189.

[13] Bernasconi, M.; Marra, G. L.; Benedek, G.; Miglio, L.; Jouanne, M.; Julien, C.; Scagliotti, M.; Balkanski, M. Lattice dynamics of layered MPX_3 (M=Mn,Fe,Ni,Zn;X=S,Se) compounds. *Phys. Rev. B* **1988**, *38*, 12089–12099.

[14] Strasdas, J. et al. Electronic Band Structure Changes across the Antiferromagnetic Phase Transition of Exfoliated $MnPS_3$ Flakes Probed by μ-ARPES. *Nano Lett.* **2023**, *23*, 10342.

[15] Kim, S. Y. et al. Charge-Spin Correlation in van der Waals Antiferromagnet NiPS3. *Phys. Rev. Lett.* **2018**, *120*, 136402.

[16] Hüfner, S. *Photoelectron Spectroscopy: Principles and Applications*; Advanced Texts in Physics; Springer Berlin Heidelberg, 2013.

[17] Sobota, J. A.; He, Y.; Shen, Z.-X. Angle-resolved photoemission studies of quantum materials. *Rev. Mod. Phys.* **2021**, *93*, 025006.

[18] Brec, R. Review on structural and chemical properties of transition metal phosphorous trisulfides MPS_3. *Solid State Ionics* **1986**, *22*, 3 – 30.

[19] Zhang, H.; Pincelli, T.; Jozwiak, C.; Kondo, T.; Ernstorfer, R.; Sato, T.; Zhou, S. Angle-resolved photoemission spectroscopy. *Nat. Rev. Methods Primers* **2022**, *2*, 54.

[20] Momma, K.; Izumi, F. *VESTA3* for three-dimensional visualization of crystal, volumetric and morphology data. *J. Appl. Crystal.* **2011**, *44*, 1272–1276.

[21] Lançon, D.; Ewings, R. A.; Guidi, T.; Formisano, F.; Wildes, A. R. Magnetic exchange parameters and anisotropy of the quasi-two-dimensional antiferromagnet NiPS3. *Phys. Rev. B* **2018**, *98*, 134414.

[22] Chittari, B. L.; Park, Y.; Lee, D.; Han, M.; MacDonald, A. H.; Hwang, E.; Jung, J. Electronic and magnetic properties of single-layer MPX_3 metal phosphorous trichalcogenides. *Phys. Rev. B* **2016**, *94*, 184428.

[23] Scheie, A.; Park, P.; Villanova, J. W.; Granroth, G. E.; Sarkis, C. L.; Zhang, H.; Stone, M. B.; Park, J.-G.; Okamoto, S.; Berlijn, T.; Tennant, D. A. Spin wave Hamiltonian and anomalous scattering in NiPS3. *Phys. Rev. B* **2023**, *108*, 104402.

[24] Trimarchi, G.; Wang, Z.; Zunger, A. Polymorphous band structure model of gapping in the antiferromagnetic and paramagnetic phases of the Mott insulators MnO, FeO, CoO, and NiO. *Phys. Rev. B* **2018**, *97*, 035107.

[25] Zhang, P.; Richard, P.; Qian, T.; Xu, Y.-M.; Dai, X.; Ding, H. A precise method for visualizing dispersive features in image plots. *Rev. Sci. Instr.* **2011**, *82*, 043712.

[26] Tsai, D.-M.; Chen, M.-F. Curve fitting approach for tangent angle and curvature measurements. *Pattern Recognition* **1994**, *27*, 699–711.

[27] Rohrbach, A.; Hafner, J. Molecular adsorption of NO on NiO(100): DFT and DFT + U calculations. *Phys. Rev. B* **2005**, *71*, 045405.

[28] Cococcioni, M.; de Gironcoli, S. Linear response approach to the calculation of the effective interaction parameters in the LDA + U method. *Phys. Rev. B* **2005**, *71*, 035105.

[29] Panda, S. K. et al. High photon energy spectroscopy of NiO: Experiment and theory. *Phys. Rev. B* **2016**, *93*, 235138.

[30] Kuneš, J.; Anisimov, V. I.; Skornyakov, S. L.; Lukoyanov, A. V.; Vollhardt, D. NiO: Correlated Band Structure of a Charge-Transfer Insulator. *Phys. Rev. Lett.* **2007**, *99*, 156404.

[31] Craco, L.; Leoni, S. Normal-state correlated electronic structure of the tetragonal $TlNi_2Se_2$ superconductor. *Phys. Rev. B* **2023**, *108*, 045140.

[32] Krukau, A. V.; Vydrov, O. A.; Izmaylov, A. F.; Scuseria, G. E. Influence of the exchange screening parameter on the performance of screened hybrid functionals. *The Journal of Chemical Physics* **2006**, *125*, 224106.

[33] Heyd, J.; Scuseria, G. E.; Ernzerhof, M. Hybrid functionals based on a screened Coulomb potential. *The Journal of Chemical Physics* **2003**, *118*, 8207–8215.

[34] Perdew, J. P.; Ernzerhof, M.; Burke, K. Rationale for mixing exact exchange with density functional approximations. *The Journal of Chemical Physics* **1996**, *105*, 9982–9985.

[35] Shishkin, M.; Kresse, G. Implementation and performance of the frequency-dependent *GW* method within the PAW framework. *Phys. Rev. B* **2006**, *74*, 035101.

[36] Hybertsen, M. S.; Louie, S. G. Electron correlation in semiconductors and insulators: Band gaps and quasiparticle energies. *Phys. Rev. B* **1986**, *34*, 5390–5413.